A human dynein heavy chain mutation impacts cortical progenitor cells causing developmental defects, reduced brain size and altered brain architecture

Delfina M Romero, Donia Zaidi, Carmen Cifuentes-Diaz, Camille Maillard, Gael Grannec, Mohammed Selloum, Marie-Christine Birling, Nadia Bahi-Buisson, Fiona Francis

HAL Id: hal-04058455

https://hal.sorbonne-universite.fr/hal-04058455

Submitted on 4 Apr 2023

A human dynein heavy chain mutation impacts cortical progenitor cells causing developmental defects, reduced brain size and altered brain architecture

Delfina M. Romero [a,b,c,1,2], Donia Zaidi [a,b,c,1], Carmen Cifuentes-Diaz [a,b,c], Camille Maillard [d,e], Gael Grannec [a,b,c], Mohammed Selloum [f,g,h,i,j], Marie-Christine Birling [f,g,h,i,j], Nadia Bahi-Buisson [d,e,k,l], Fiona Francis [a,b,c,*]

[a] INSERM UMR-S 1270, F-75005 Paris, France
[b] Sorbonne University, F-75005 Paris, France
[c] Institut du Fer à Moulin, F-75005 Paris, France
[d] Laboratory of Genetics and Development of the Cerebral Cortex, INSERM UMR-S 1163, Imagine Institute, Paris, France
[e] Paris Descartes-Sorbonne Paris Cité University, Imagine Institute, Paris, France
[f] Institut de Génétique et de Biologie Moléculaire et Cellulaire, Illkirch, France
[g] Centre National de la Recherche Scientifique, UMR7104, Illkirch, France
[h] Institut National de la Santé et de la Recherche Médicale, U964 Illkirch, France
[i] Université de Strasbourg, Illkirch, France
[j] CELPHEDIA, PHENOMIN, Institut Clinique de la Souris (ICS), Illkirch-Graffenstaden, France
[k] Pediatric Neurology APHP- Necker Enfants Malades University Hospital, Paris, France.
[l] Centre de Référence, Déficiences Intellectuelles de Causes Rares, APHP- Necker Enfants Malades University Hospital, Paris, France

ARTICLE INFO

ABSTRACT

Dynein heavy chain (*DYNC1H1*) mutations can either lead to severe cerebral cortical malformations, or alternatively may be associated with the development of spinal muscular atrophy with lower extremity predominance (SMA-LED). To assess the origin of such differences, we studied a new *Dync1h1* knock-in mouse carrying the cortical malformation p.Lys3334Asn mutation. Comparing with an existing neurodegenerative *Dync1h1* mutant (*Legs at odd angles*, *Loa*, p.Phe580Tyr/+), we assessed Dync1h1's roles in cortical progenitor and especially radial glia functions during embryogenesis, and assessed neuronal differentiation.

p.Lys3334Asn /+ mice exhibit reduced brain and body size. Embryonic brains show increased and disorganized radial glia: interkinetic nuclear migration occurs in mutants, however there are increased basally positioned cells and abventricular mitoses. The ventricular boundary is disorganized potentially contributing to progenitor mislocalization and death. Morphologies of mitochondria and Golgi apparatus are perturbed *in vitro*, with different effects also in *Loa* mice. Perturbations of neuronal migration and layering are also observed in p. Lys3334Asn /+ mutants. Overall, we identify specific developmental effects due to a severe cortical malformation mutation in *Dync1h1*, highlighting the differences with a mutation known instead to primarily affect motor function.

1. Introduction

Cerebral cortical neurons are localized in the outer regions of the brain and are involved in advanced cognitive functions in human (Frith, 1996). During cortical development, progenitor proliferation and neuronal migration are tightly regulated, and alteration of these processes can lead to cortical malformations, such as lissencephaly ('smooth brain') and microcephaly ('small brain') (Romero et al., 2018; Subramanian et al., 2020). Cortical malformations are commonly associated with intellectual disability, epilepsy and neuropsychiatric disorders (Parrini et al., 2016).

Radial glial cells (RG) derive from neuroepithelial cells and are key progenitors involved in cortex development, able to amplify and to give birth to other cell types during corticogenesis (Rakic et al., 2009). Their unique morphology includes a bipolar shape, with a short apical process facing the ventricle and a long basal process extending to the pial surface. The latter acts as a support for neuronal migration (Rakic, 1972; Borrell and Götz, 2014). RG somata, expressing the transcription factor Pax6, are restricted to the ventricular zone (VZ), where their nuclei move in a cell-cycle dependent manner. This nuclear movement, requiring microtubule motor proteins, is termed interkinetic nuclear migration (INM) (Spear and Erickson, 2012).

Dynein is a motor protein with an oriented trajectory towards the minus end of microtubules (Paschal and Vallee, 1987). This protein complex is mainly composed of two heavy, two intermediate, two light-intermediate and two light chains (Mizuno et al., 2007). Cytoplasmic dynein is involved in a variety of intracellular transport mechanisms, such as the movement of vesicles and organelles, including the nucleus, as well as the assembly and maintenance of structures such as the mitotic spindle and the Golgi apparatus (Schiavo et al., 2013). In cultured blastocysts, when dynein heavy chain is absent, the Golgi apparatus becomes fragmented and in addition to endosomes and lysosomes, shows an abnormal localization (Harada et al., 1998). Dynein was also shown to play a role in retrograde transport in neurons (He et al., 2005). In RG progenitors of the developing cortex, dynein, together with its cargo adaptor Bicaudal D2 (Bicd2), plays a role in INM, allowing the basal to apical descent of the nucleus in G2 phase (Tsai et al., 2010; Hu et al., 2013). Indeed, this G2 apical descent requires the targeting of dynein to the nuclear envelope (NE): first the nucleoporin RanBP2 recruits BicD2, which recruits dynein and its regulatory complex dynactin to the nuclear surface (Splinter et al., 2010; Splinter et al., 2012). Then, the nucleoporin Nup133, recruits CENP-F (Bolhy et al., 2011) which in turn, recruits NudE and NudEL, binding directly to dynein and its regulator LIS1. Thus, apical descent of RG nuclei occurs in two steps *via* dynein (Hu et al., 2013).

Heterozygous mutations were found in the dynein heavy chain gene (*DYNC1H1*) in patients with cortical malformations, in a spectrum ranging from microcephaly with dysgyria to lissencephaly (Poirier et al., 2013). Other mutations in *DYNC1H1* were also previously identified in peripheral neuropathies, such as spinal muscular atrophy with lower extremity dominance (SMA-LED), characterized by muscle weakness (Schiavo et al., 2013; Garrett et al., 2014). This protein has two domains, an N-terminal tail and a C-terminal motor domain (Schiavo et al., 2013). Previous evidence suggested that mutations affecting the tail domain are often associated with peripheral neuropathies such as SMA-LED, whereas mutations found in the motor domain are commonly associated with cortical malformations (Schiavo et al., 2013). However, this correlation is not always as expected and some patients also show both disorders (Wiggins et al., 2012; Schiavo et al., 2013). Overall though it is likely that particular mutations are each associated with a distinct phenotype, according to the impact of the mutation on dynein's function.

Previously characterized *Dync1h1* mouse models have shown motor and sensory anomalies (Schiavo et al., 2013). This includes *Legs at odd angles* (*Loa*), exhibiting a mutation in the tail domain (Phe580Tyr/ F580Y) (El-Kadi et al., 2010; Wiggins et al., 2012; Schiavo et al., 2013).

New models are required to characterize the cortical defects when *Dync1h1* is mutated. A *de novo* missense mutation pLys3336Asn (K3336N) in the *DYNC1H1* motor domain was found in a patient exhibiting predominantly cortical malformations, with microcephaly and dysgyric features (Poirier et al., 2013). K3336N is associated specifically with microcephaly, posterior pachygyria, frontal polymicrogyria, other CNS malformations and early-onset epilepsy (Poirier et al., 2013; Schiavo et al., 2013). Modeling this robust cortical malformation mutation, for which *in vitro* data exists (Hoang et al., 2017), is expected to further identify dynein-related mechanisms leading to cortical disorders.

We present here a new knock-in mouse model, K3334N, exhibiting the mutation equivalent to the cortical malformation mutation, K3336N, in human. This new model allowed us to characterize the impact of this mutation on dynein functions in the developing cortex. Using cellular studies *in vitro* and *in vivo*, we determined cortical phenotypes, especially focusing on neuronal progenitors, to help explain the microcephaly and dysgyria observed in patients. We studied the effect of this mutant allele on cell proliferation and localization, INM, neuronal migration and organelle structural integrity, such as the Golgi apparatus and mitochondria. These mice can be distinguished from other *Dync1h1* mutants due to the severe cortical defects identified in the heterozygous state, and they hence represent a pertinent model mimicking the cortical malformation in Human.

2. Materials and methods

2.1. Animals

Research was carried out conforming to national and international directives (directive 2010 CE/63 / EU, French national APAFIS n ° 8199) with protocols followed and approved by the local ethical committee (Charles Darwin, Paris, France). The mouse model was created at the PHENOMIN MCI/ICS (Mouse Clinical Institute - Institut Clinique de la Souris, Illkirch, France; http://www-mci.u-strasbg.fr), with protocols approved by the local animal care, use and ethic committee of the Institute of Genetics and of Molecular and Cellular Biology (IGBMC) under accreditation number 2012–139. Mice were housed with a light/ dark cycle of 12 h (lights on at 07:00). Males and females were used in all analyses. The following lines were used: Loa/+ (C3H), EM:01847 - Dync1h1 < Loa>/H - 8085 - (RQ:003139, obtained from the MRC Harwell Institute), L3/+ and L2/+ knock-in lines.

2.2. Generation of a Dync1h1 mouse K3334N knock-in (KI) line

The KI mouse line was established at the Mouse Clinical Institute - Institut Clinique de la Souris, (Illkirch, France; http://www-mci.u-stras bg.fr), in the framework of the European project Gencodys (http ://www.gencodys.eu/). This line was generated and analyzed on the C57BL/6 N (B6N) genetic background. The mouse model was generated by homologous recombination in embryonic stem (ES) cells using a targeting vector containing regions homologous to the genomic *Dync1h1* sequences and the p.(Lys3334Asn) variant. LoxP sites surrounding the exon of interest (exon 52) were first introduced into a genomic DNA targeting construct. This vector contained a neomycin cassette encompassed by two FRT sites upstream of the second loxP site (see Fig. 1A-B). This targeting construct was introduced by electroporation to allow homologous recombination in B6N ES cells. After G418 selection, targeted clones were identified by long-range PCR using external primers and further confirmed by Southern blot with an internal Neomycin probe as well as 5′ and 3′ external probes. Two positive ES clones were injected into B6N blastocysts. Resulting male chimeras (L3 line) were bred with wild type (WT) B6N females to obtain germline transmission. L3 heterozygote mice are viable, fertile and overall healthy, and are born in appropriate mendelian ratios. Sanger sequencing confirmed the presence of the missense mutation (Suppl. information). We performed

Fig. 1. K3334N mutant mice are smaller and brain architecture is altered. (A) Alignment of human and mouse sequences in the K3336 region. Mutant residue indicated in pink. (B) Schematic representation of dynein heavy chain and localization of studied mutations (*Loa* mutation in the tail domain and K3334N/K3336N mutation in the motor domain). (C) Schematic representation of WT, L3 and L2 alleles and resulting mice. (D) Photography of P0 (left) and P6 (right) mice. Scale: 1 cm. (E) Graphical representation of P24 weight. Statistical test: One-way ANOVA, post-test Dunn's multiple comparison, ** $p < 0.01$. (F) Photography of P0 brains. Arrow indicates malformed and smaller hemisphere in L2/+ mouse. Scale: 0.5 cm. (G) Micrograph of coronal sections at P0. Scale bar: 100 μm. (H-J) Measurements are shown of whole hemisphere area, brain area excluding ventricle, and ventricle area. Statistical test: One-way ANOVA, post-test Dunn's multiple comparison, * $p < 0.05$. (K) Image of E14 brains and graphical representation of the cortical wall thickness. (L) Quantifications of the relative cortical wall thickness at E14.5. One-way ANOVA, post-test Dunn's multiple comparison, * $p < 0.05$. At least 4 individuals from 3 different litters per age and genotype. (For interpretation of the references to colour in this figure legend, the reader is referred to the web version of this article.)

initial crosses between L3/+ and *pCAG*-Flpo/+ deleter mice to remove the neo cassette (Birling et al., 2012). After initial crosses, L3/+ mice were then crossed with an Act-Flpase deletor mouse line (B6.Cg-Tg (ACTFLPe)9205Dym/J) to remove the neo cassette, gratefully obtained from Bernadette Drayton-Libotte and Frédéric Relaix, Créteil, *via* the TAAM repository (Orléans, France). Flpase/+ expression, under the control of the *Actb* promoter, is detected as early as embryonic day 10 (Rodríguez et al., 2000). New L2 mice were thus generated for each set of experiments.

Representative images in Fig. 1 did not include L3/+, if quantifications revealed no differences compared to WT.

2.3. Crosses and genotyping

Heterozygous *Loa*/+ mice were crossed to controls WT (C3H) mice (day of plug = E0.5) to obtain *Loa*/+ and littermate controls WT (C3H). *Loa* homozygous mice are not viable. Genotyping was performed by polymerase chain reaction (PCR). The following primers were used for *Loa*/+ genotyping: primer F: ATTGAGGAGGTGAACCTGGCC, primer R: CAGTCATCGAAGATCTCCTGGG. Following the amplification, PCR products were digested with the restriction enzyme *Rsa*I for 1 h at 37 °C, and then resolved in a 2% agarose gel to identify the genotypes (Wiggins et al., 2012). Heterozygous L3/+ mice were crossed to Act-Flpase mice (C57BL/6 N) mice (day of plug = E0.5) to obtain L3/+, L2/+ and littermate control WT (Flp/+ or +/+) mice (C57BL/6 N). Genotyping was performed by PCR, using a three-primer strategy, Ef: GCACATCTGGGAGAGGCTCTGC, Mqr: TGCTAAAGCGCATGCTCCAGACTGC, Er: CATGCAAGACAAGTAAAGGGCTAGCAC.

2.4. Antibodies

Primary antibodies used were: polyclonal rat anti-BrdU (BU1/75 (ICR1), BioRad, 1:1000); polyclonal rabbit anti-Pax6 (PRB—278P, Covance, 1:300), rabbit anti-Tbr2 (AB23345, Abcam, 1:300), polyclonal rabbit anti-dynein HC (Sc9115 (R-325), Santa Cruz, 1:200), rabbit anti-BICD2 (HP023013, Sigma, 1:500), rabbit anti-PH3 (Millipore, 06–570, 1:400), rat anti- Ctip2 (clone 25B6, ab18465, Abcam 1:500); monoclonal mouse anti–Ki-67 (556003, BD Bioscience, 1:200), rabbit anti––caspase-3 (559565, BD, 1:250); mouse anti-nestin (ab6142, Abcam, 1:600), mouse anti-GM130 (6100822, BD, 1:300), mouse anti-Satb2 (ab51502, Abcam, 1:500), mouse anti-GAPDH (6004–1-Ig, Proteintech,1:500), mouse anti-tubulin (clone DM1A, Sigma-Aldrich,1:10000) and F-actin was labeled with phalloidin (A30107, Invitrogen, 1:200).

Secondary antibodies used for immunohistochemistry were: goat anti-rat Alexa 568 (Invitrogen, 1:800); goat anti-rabbit Alexa 568 (Invitrogen, 1:800); goat anti-mouse Alexa 633 (Invitrogen, 1:800). Secondary for Western blot: Dylight anti-mouse 800, anti-rabbit 680, anti-rabbit 800 (ThermoFisher, 1:10000).

2.5. Mouse neuronal progenitor primary cell culture

The neuronal progenitor cell cultures were adapted from Sun et al. (2011), giving highly enriched populations of Pax6(+) cells. Briefly, 6-well cell culture plates were coated with Poly-ᴅ-lysine (PDL, P6407, Sigma Aldrich) 2 μg/cm2 in sterile 1 x PBS, O/N, at 37 °C and 5% CO2. The following day, the PDL was removed, and the plates were coated with 1 μg/cm2 fibronectin (F1141, Sigma Aldrich) in sterile 1 x PBS. E14.5 timed-pregnant mice were sacrificed by cervical dislocation and the uterus was placed in ice cold basal medium (DMEM/F12 Hams, 21,041, Thermo Fisher, 1% Pen-Strep (Gibco), 2.9 mg/ml glucose and 1.2 mg/ml sodium bicarbonate). Embryos were collected and the cortex from both hemispheres was dissected and kept at 4 °C in basal medium. The medium was removed and substituted by pre-warmed sterile complete medium (basal medium complemented with 1 x B27 without vitamin A (12589–010, Gibco), 20 ng/ml of EGF (E9644, Sigma Aldrich)

and 20 ng/ml of FGF (F0291, Sigma Aldrich). The tissue was dissociated and each sample was centrifuged (3 min, 1000 rcf). The medium was removed and substituted by fresh pre-warmed complete medium followed by re-suspension of the cells. 1×10^5 cells were plated in coated 6-well culture plates.

Cells were split once at seven days *in vitro* (DIV) before performing experiments. Half of the culture medium was changed by fresh complete medium every 2 days for one week. For splitting, cells were washed with pre-warmed Versene (Gibco), followed by a 3 min incubation with pre-warmed StemPro Accutase (Gibco) at 37 °C. Cells were plated (6–8 $\times$ 10^5) on coated 14 mm glass coverslips and cultured for 4 DIV for immunocytochemistry experiments.

2.6. DNA and RNA extraction from progenitor cells

DNA was extracted from cultures of mouse neuronal progenitor cells using QuickExtract™ DNA Extraction Solution (LU-QE09050, Euromedex). Briefly, the solution was added to pelleted cells and these were incubated 7 min at 65 °C and 2 min at 98 °C.

Total RNA was extracted from progenitor cells using the Qiagen RNeasy kit (74,104, Qiagen). Cells were lysed by a mix of RLT buffer, β-Mercapto-ethanol and 70% ethanol. Lysates were transferred onto columns, followed by a short centrifugation, then DNase I treatment (79,254, Qiagen) and washing steps were performed. Elution was performed with RNase-free water and the RNA concentration was measured by NanoDrop 2000 (Thermo Scientific).

2.6.1. RT-qPCR
Before proceeding to Real Time-qPCR, 500 ng of RNA were retro-transcribed using the Verso cDNA Synthesis kit (AB-1453/B, Thermo-Scientific) following manufacturer's instructions.

RT-qPCR reactions were performed with the GoTaq® qPCR SyberGreen

Master Mix (A6001, Promega) on an Eppendorf realplex² thermocycler. The following primers were used for RT-qPCR: Dync1h1 forward, 5′-CCAACAGCTTGGCGTTCAT-3′; Dync1h1 reverse, 5′-GGGACGACACTGGCTTGTCT-3′ (Di Pizio et al., 2023), β-actin forward, 5′-CCCTCACGCCATCCTGCGTC-3′; reverse, 5′-GCGGCAGTGGCCATCTCCTG-3′ (Gacem et al., 2020).

2.6.2. Sanger sequencing
PCR products were sequenced using the BigDye™ Terminator v3.1 Cycle Sequencing Kit (4336919, Applied Biosystems) on a Hitachi 3500xL Genetic Analyzer (Applied Biosystems) with the following primers: Dync1h1-ex52 forward, 5′- GTCCATCAAGAAGCAGCACC-3′; Dync1h1-ex52 reverse 5′- CAGCCGAGAAGTTGACGATG-3′; Dync1h1-ex53 reverse 5′-CCCACTTCACCATAGGACCA-3′; NeoR reverse 5′-CCTGATGCTCTTCGTCCAGA-3′.

2.7. Western blot

Samples were denatured with 2× NuPAGE LDS Buffer (Thermo-Fisher) for 10 min at 70 °C. Denaturing electrophoresis was performed on a 4%–12% Bis-Tris Gel with MOPS SDS running buffer for 2 h at 110 V. Proteins were transferred onto nitrocellulose membranes for 1 h at 110 V and 4 °C in a Tris-Glycine transfer buffer (Tris 25 mM, Glycine 192 mM, ethanol 10%). After protein transfer, the membranes were stained with Ponceau red to check the transfer quality. The membranes were extensively washed with distilled water, followed by a 60 min incubation in TBST 1× (100 mM Tris pH 7.5, 150 mM NaCl, 10% ethanol, 0.05% Tween) + 5% milk. Incubation of 45 min in the dark with the secondary antibody was performed to identify non-specific binding sites. The primary antibody was incubated O/N at 4 °C, and abundantly washed with TBST 1×, followed by incubation with the secondary antibody (see above). After extensive washes in TBST then with TBS 1×, the membranes were scanned using an Odyssey (Li-Cor)

infrared scanner.

2.8. Immunocytochemistry

Cells were washed in 1 x PBS prior to fixation with 4% *w/v* PFA in 0.1 M phosphate buffer, pH 7.4, for 15 min at RT. The cells were extensively washed in 1 x PBS followed by a 15 min wash in PBST 0.2% (Triton X-100 0.1% in 1 x PBS). Incubation with blocking solution (10% Normal goat serum (NGS) ThermoFisher, 0.1% Triton X-100 in 1 x PBS) was performed for 1 h at RT and the following primary antibodies were applied for 2 h at RT or O/N at 4 °C with GM130 or Pax6 (see above for antibodies' references). The cells were extensively washed with blocking solution and the following secondary antibodies were incubated for 2 h at RT in the dark. After washes, Hoechst (1:10000, ThermoFisher) was applied for 15 min at RT in the dark. The cells were extensively washed in PBS and the coverslips mounted with Fluoromount G (Southern Biotechnology). Images were acquired with a TCS Leica SP5-II confocal microscope.

2.9. MitoTracker red CMXRos labeling

A solution of complete culture media containing 100 nM of the red fluorescent MitoTracker Red CMXRos dye (Invitrogen, M7512). Cells in this solution were then incubated for 30 min at 37 °C in a 5% C02 incubation chamber. Coverslips were rinsed abundantly in PBS 1× before fixation with PFA 4% in PBS and Hoechst staining as previously described. Mitotracker fluorescence was monitored with a laser scanning TCS Leica SP5-II confocal microscope equipped with a Plan-Apochromat 63× oil immersion lens and 1.5× zoom, covering 20 acquisitions planes of 0.20 µm.

2.10. BrdU injections and immunohistochemistry

Pregnant female mice at E14.5 were injected with 5-bromo-2′-deoxyuridine (BrdU, 99% Bioultra, Sigma-Aldrich, 50 µg per gram body weight in PBS1×) and sacrificed after 0.5 h, 2 h, 4 h. S-phase entry evolution and interkinetic nuclear migration of RG were analyzed. Embryonic brains were fixed by immersion O/N at 4 °C in 4% *w/v* PFA in 0.1 M phosphate buffer, pH 7.4, followed by extensive washes in 1 x PBS. Brains were cut in 70 µm thick coronal sections using a vibrating blade microtome (Leica VT1000 S).

In order to label BrdU+ nuclei, we performed immunohistochemistry on floating brain slices. Briefly, slices were permeabilized with PBST1x during 15 min, then DNA was denatured with hydrochloric acid (HCl) 2 N treatment during 30 min at 37 °C. After washes, blocking was performed for 1 h at RT with 1× PBS containing 10% NGS and 0.1% Triton X-100 before incubation O/N at 4 °C with the primary antibody. After extensive washes, sections were incubated with the secondary antibody for 2 h at RT protected from the light. This was followed by 10 min incubation in Hoechst (ThermoFisher, 1:10000) and washed with 1× PBS. F-actin was labeled with phalloidin (1:200) diluted in PBS and incubated 1 h at RT. Brain slices were finally mounted with Fluoromount G (Invitrogen).

For Pax6, PH3, Tbr2, Nestin, Satb2 and active caspase-3 immunolabeling the same protocol was followed without DNA denaturation treatment. For Tbr2 and active caspase 3, we performed antigen retrieval by incubating the sections in sodium citrate 10 mM pH 6 at 95 °C for 20 min and allowing them to cool down before blocking. Then slices were incubated with secondary antibodies and mounted with Fluoromount G.

In order to perform immunohistochemistry combining the primary antibodies mouse anti-Ki67 and rat anti-BrdU, antigen retrieval was performed by incubating the sections in sodium citrate 10 mM pH 6 at 95 °C for 20 min and allowing them to cool before blocking. Blocking was performed for 1 h at RT with 1× PBS containing 10% NGS (Normal Goat Serum, ThermoFisher) and 0.1% Triton X-100 before incubation

for 48 h at 4 °C with the primary antibody (Ki67, proliferation marker). After extensive washes, sections were incubated with the secondary antibody for 2 h at RT in the dark. Then sections were fixed with 8% PFA *w/v* for 15 min at RT (Palmer et al., 2000). Extensive washes with PBST 0.1% (1× PBS and 0.1% Triton X-100) were performed, followed by incubation in HCl 2 N for 30 min at 37 °C. After extensive washes, the sections were incubated with the primary antibody (BrdU), secondary antibody, Hoechst, and then mounted with Fluoromount G (as previously described).

2.10.1. Neuronal progenitors entering S-phase of the cell cycle

The calculation for S-phase entry was performed considering total BrdU nuclei after mice injections between 0.5 h and 2 h. Briefly, we subtracted the number of BrdU+ cells after 0.5 h from the number of BrdU labeled nuclei after 2 h (mean ± SEM). Thus, we could estimate the number of cells entering in S phase between 0.5 h to 2 h, expressed as %.

2.11. In utero electroporation (IUE)

Timed-pregnant mice (E14) were anesthetized with isoflurane (4% during induction and 2–2.5% during surgery) and embryos exposed within the intact uterine wall after sectioning the abdomen. Embryos were constantly hydrated with NaCl 0.9% (B. Braun). A solution containing DNA (1 µg/µl) and 20% w/v fast green in sterile *endo*-free water was injected in the lateral ventricles of the embryos. A pCAG-IRES-TdTomato plasmid (kindly provided by C. Lebrand, Lausanne) was electroporated. Forceps electrodes (System CUY650P5 NepaGene Co) were placed around the embryo head at a 45° angle and plasmids electroporated by discharging a 4,000-µF capacitor charged to 35 V (five electric pulses of 50 ms with 950 ms intervals) with a CUY21 NepaGene electroporator. The embryos were then placed back in the abdominal cavity for 12 h for subsequent analyses.

Brain sections (70 µm thick) from *in utero* electroporation experiments were exclusively incubated with Hoechst and extensively washed before mounting. IHC was performed as previously described, using the primary polyclonal rabbit anti-Ds-red antibody (Clontech, USA, #632496, 1:400) and secondary Alexa-568 (ThermoFisher).

2.12. Electron microscopy

Mouse Pax6(+) neuronal progenitor cells were fixed for 1 h in 0.1 M phosphate buffer containing 4% PFA and 2.5% glutaraldehyde at 4 °C. Then cells were post-fixed in 2% osmium tetroxide diluted in 0.2 M Palade buffer (Palade, 1952). After osmication, cells were dehydrated in several ethanol baths and flat-embedded using an epoxy resin (EPON 812, Polysciences). Small pieces were dissected from flat embedded cultures after resin polymerization, mounted in plastic stubs and sectioned in ultrathin sections (50 nm). Finally, sections were stained with uranyl acetate and lead citrate and examined using a Philips CM100 electron microscope. Digital images were obtained with a CCD camera (Gatan Orius).

2.13. Image acquisitions

After immunohistochemistry, images were acquired with a confocal microscope SP5 (Leica) using a 40× objective with the same conditions for each section. A total thickness of 10 µm was covered with 33 acquisitions of 0.30 µm. For immunocytochemistry, acquisitions were carried out using a 63× objective.

2.14. Quantification and statistical analysis

2.14.1. RT-qPCR

RT-qPCR results were analyzed using the 2-ddCT method where the relative abundance values of each amplification product were

normalized to β-actin, and mRNA expression levels in the mutants were expressed relative to WT.

2.14.2. Immunohistochemistry and Immunocytochemistry images

For immunohistochemistry analyses ImageJ was used. Cell counting was done manually using the cell counter plugin.

For Golgi apparatus analyses ImageJ was used. Golgi analyses were performed with the plugin 3D Object Counter, covering 20 acquisitions planes of 0.20 μm. Golgi elements morphological parameters were calculated for a minimum of 25 cells per embryo, with 3 embryos studied per genotype. Mitochondrial analyses were performed using ImageJ. Mitochondrial morphological parameters were calculated for a minimum of 15 cells per embryo, with 3 embryos studied per genotype.

2.14.3. F-actin fluorescence intensity measurement

F-actin fluorescence intensity was measured along the ventricular surface (100 μm) by drawing a free hand line. The plot profile was given *via* ImageJ and the results were presented in Log10. The same acquisition and image processing parameters were used between each images.

2.14.4. Western blot

For Dynein and BicD2 analyses, band intensity was measured and normalized to GAPDH or tubulin using ImageJ.

2.14.5. Statistical analysis

Statistical tests were carried out using GraphPad Prism 5. A *P* value <0.05 was considered significant. For each experiment, the specific test used is described in the figure legend. Data were collected and processed randomly.

3. Results

3.1. Reduced viability and size of dynein K3334N knock-in (KI) mutants

Generation and crossing of mice strongly suggested that the K3334N mutation in the homozygous state is lethal (0 homozygous pups generated in 10 litters from heterozygous x heterozygous crosses). We hence studied heterozygous mice, similar to the mutation status in human patients (Poirier et al., 2013). Note that human and mouse dynein sequences are highly conserved (Fig. 1A). We first generated heterozygous mice retaining the Frt-flanked neomycin (neo) cassette, K3334N(Neo)/WT, termed here simply L3/+ (Fig. 1B-C), and observed that they survived and reproduced normally. We next performed crosses between L3/+ and p*Actb*-Flpe/+ deleter mice to remove the neo cassette (Rodríguez et al., 2000), allowing us to assess the development of the resulting neoremoved K3334N mutants (K3334N/WT; Flp+/WT, termed here L2/+), in comparison with littermate L3/+ and WT embryos and pups (Fig. 1C). We found that the KI neoremoved heterozygotes (L2/+) do not survive past 3–4 weeks. We further assessed the expression of Dync1h1 in WT, L3/+ and L2/+ primary cultures of cortical progenitors. Western blot analyses showed non-significant changes of protein levels among genotypes, although a noticeable trend of 26% reduction was found in the L2/+ condition (Supplementary Fig. 1A). L3/+ and *Loa*/+ mice (F580Y/WT) showed more variability with no obvious overall changes in Dync1h1 protein expression levels, although there was a potential tendency for increase in *Loa*/+ brains. We also assessed BicD2 expression (an important protein partner of dynein) in these lysates. L3/+ cells showed a significant increase in protein levels (39%) and an opposite trend was found in L2/+ cells which showed a reduction (29%) in BicD2 (Supplementary Fig. 1B). *Loa*/+ cells once again showed a non-significant tendency for increased BicD2 expression (Supplementary Fig. 1B). Finally, we compared relative Dync1h1 mRNA expression levels by RT-qPCR from neuronal progenitor cultures showing non-significant differences between WT and L3/+ mutant conditions (Supplementary Fig. 1C). Specific RT-PCRs using a forward primer in exon 52 and a reverse primer in the neo cassette, or in exon 53, followed by

sequencing, showed however, some hybrid neocontaining mutant transcripts in L3/+ progenitors (Supplementary information).

Postnatal observation of L2/+ mice strongly suggested that these animals present developmental defects. Indeed, they were noticeably smaller in size at P0 and in the early postnatal period (Fig. 1D) and at P24 their body weight was significantly lower than WT and L3/+ littermates (Fig. 1E). The latter were approximately twice the weight of L2/+ mice, which were easily recognizable in their home-cage, since they also moved less than littermates and with an unusual gait (Supplementary video 1). At earlier stages, L2/+ animals also walked in an abnormal manner: observations performed at P4 suggested walking difficulties in young L2/+ pups, and they showed visible trembling movements (Supplementary video 2). *Loa*/+ animals exhibit motor defects at 3 months, *e.g.* defects in motor coordination and less strength in the front and hind limbs (Ilieva et al., 2008). These defects were not detected in younger *Loa*/+ animals in our study (data not shown).

3.2. KI mice show a severe cortical malformation

Global L2/+ brain size at P0 appeared smaller with an architecture not as well defined as WT and L3/+ brains (Fig. 1F). P0 coronal brain sectioning and area measurements confirmed that the L2/+ hemisphere area was significantly reduced (by 22% WT *versus* (*vs*) L2/+ and 15% L3/+ *vs* L2/+). Brain area (without taking into account the ventricles) also appeared reduced in L2/+ pups (WT *vs* L2/+ by 22% and L3/+ *vs* L2/+ by 14%). These data (Fig. 1G-J) suggest brain development defects. No significant brain or hemisphere area differences were found in L3/+ compared to WT animals.

We compared the developing cortices of L2/+ with L3/+ and WT littermate embryos and pups, and we also further assessed the brain phenotype of *Loa*/+ heterozygote mice for comparison. Indeed, a previous study of the *Loa* mouse in the homozygous state reported neuronal migration defects (Ori-McKenney and Vallee, 2011), but no major cortical defects were identified in *Loa*/+ heterozygotes. Cortical wall thickness was assessed at mid-corticogenesis (E14.5). The cortical wall of L2/+ embryos was significantly thinner compared to WT (20% decrease for WT *vs* L2/+) (Fig. 1K-L). The cortical wall thickness of *Loa*/+ embryonic brains was not different compared to WT littermates, nor was the brain size and architecture at P0 as expected (data not shown) (Ori-McKenney and Vallee, 2011). Thus, the initial characterization comparing L2/+, L3/+ and *Loa*/+ mice highlighted the impact of the K3334N mutation (in the absence of the neo cassette) on general, as well as specifically brain development.

Because the patient brain phenotype is associated with microcephaly and complex brain malformations,including dysgyria and polymicrogyria (PMG) (Poirier et al., 2013), we decided to further study parameters that might help explain the microcephalic (neuronal progenitor disorder) and dysgyric (neuronal migration disorder) phenotypes.

3.3. K3334N mutation alters RG and intermediate progenitor (IP) numbers and localization

Defects in progenitors can explain reduced brain size (Bizzotto and Francis, 2015), therefore we assessed RG in the L2/+ mouse brain during cortical development. Immunolabeling for Pax6, a transcription factor specific to RG (Götz et al., 1998), was performed on coronal embryonic brain sections of L2/+, L3/+ and WT mice at mid-corticogenesis (E14.5). Briefly, we divided the cortical wall in six identical bins with the lower limit of bin 1 at the apical surface and the upper limit of bin 6 at the pial surface (Fig. 2A). We first measured VZ thickness, corresponding to Pax6 cells mainly located in bins 1 and 2, relative to the cortical wall thickness of the developing somatosensory cortex (Fig. 2A-C). The VZ represented around one third of the cortical wall in WT and L3/+ embryos, however for L2/+ embryos, this proportion was significantly increased representing almost half of the
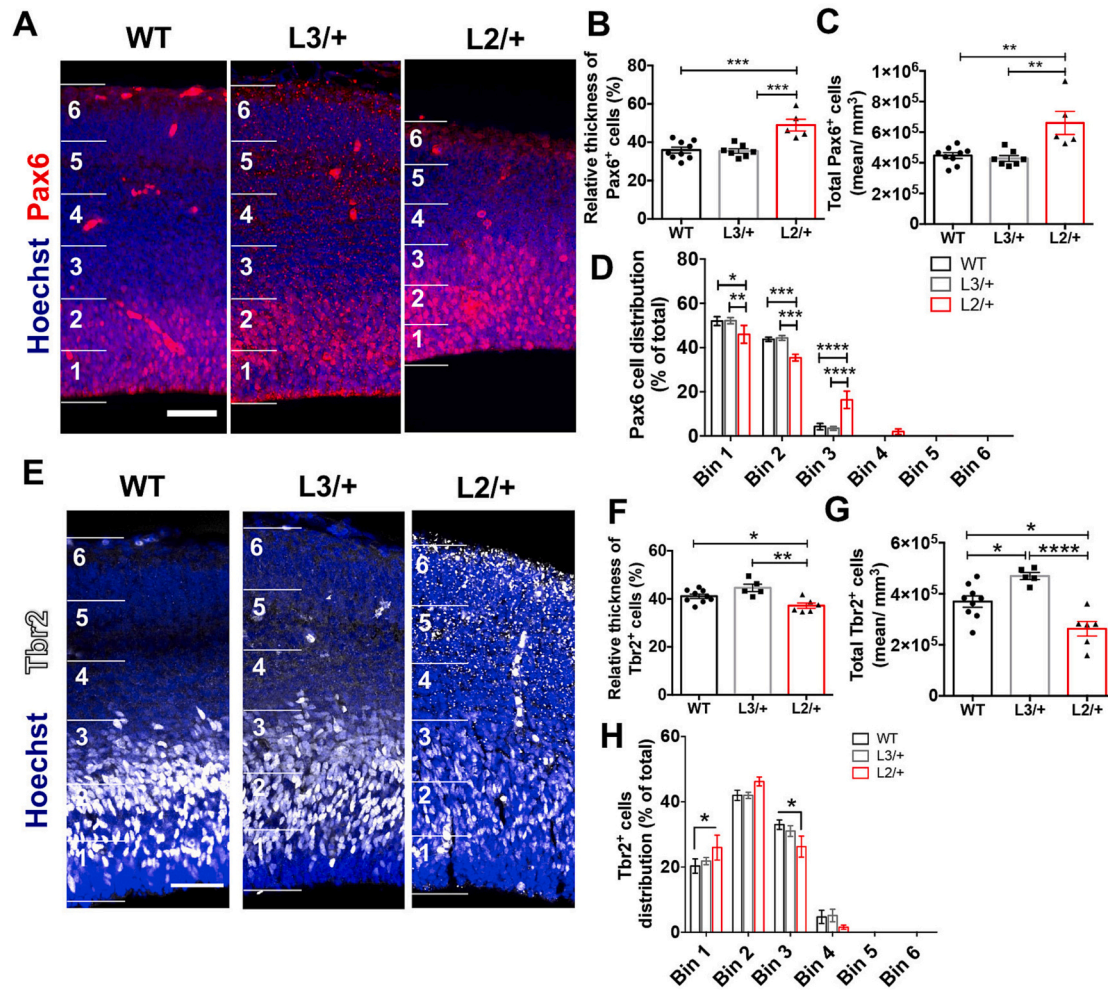
Fig. 2. K3334N mutation alters RG and intermediate progenitor (IP) counts and localization. (A) Representative images of immunolabelings for a marker of RG (Pax6 in red) on E14.5 coronal brain sections. Scale bar: 50 μm. (B) Quantifications of the relative thickness of Pax6+ cells to cortical wall thickness expressed as %. One-way ANOVA with *post hoc* Tukey's test, $F_{2, 18} = 14.34$, $p = 0.0002$ ($n = 9$ WT, $n = 7$ L3/+ and $n = 5$ L2/+ embryos). *** $p = 0.0004$. (C) Quantifications of total Pax6+ cells per volume of brain (mm^3), mean ± SEM. One-way ANOVA with *post hoc* Tukey's test, $F_{2, 18} = 10.86$, $p = 0.0008$ ($n = 9$ WT, $n = 7$ L3/+ and $n = 5$ L2/+ embryos). ** $p < 0.002$. (D) Pax6 cell distribution along the cortical wall divided in 6 equal bins. Two-way ANOVA with *post hoc* Tukey's test. Interaction Bin x genotype, $F_{10, 102} = 8.3$, $p < 0.0001$ ($n = 8$ WT, n = 7 L3/+ and n = 5 L2/+ embryos). * $p = 0.010$, ** $p = 0.0094$, *** $p < 0.0002$, **** $p < 0.0001$. (E) Representative coronal brain section images of Tbr2 immunolabelings in WT, L3/+ and L2/+ at E14.5. Scale bar: 50 μm. (F) Quantifications of the relative thickness of Tbr2+ cells to cortical wall thickness expressed as %. One-way ANOVA with *post hoc* Tukey's test, $F_{2, 17} = 9.16$, $p = 0.002$ (n = 9 WT, n = 5 L3/+ and $n = 6$ L2/+ embryos). * $p = 0.047$, ** $p = 0.0015$. (G) Quantifications of the total Tbr2+ cells per volume of brain (mean/mm^3). One-way ANOVA with *post hoc* Tukey's test, $F_{2, 17} = 15.8$, $p = 0.0001$ (n = 9 WT, n = 5 L3/+ and n = 6 L2/+ embryos). * $p < 0.024$, **** p < 0.0001. (H) Tbr2+ cell distribution across the cortical wall divided in 6 bins. Two-way ANOVA with *post hoc* Tukey's test. Interaction Bin x genotype, $F_{10, 102} = 361$, p < 0.0001; * p < 0.05. (For interpretation of the references to colour in this figure legend, the reader is referred to the web version of this article.)

cortical wall thickness (WT, 35.9% *vs* L2/+, 48.9%, and L3/+, 35.4%) (Fig. 2B). Total Pax6 positive (+) cells were also increased by 57.1% in L2/+ brains compared to WT and L3/+, and their distribution in L2/+ brains was also altered (Fig. 2C-D). The proportion of Pax6(+) cells in L2/+ was significantly reduced in bins 1 and 2 (corresponding to the apical part of the VZ) compared to WT and L3/+. Inversely, a significantly greater proportion of Pax6(+) cells was found in bin 3 compared to WT and L3/+ (4.3% WT, 3.5% L3/+ *vs* 16.4% L2/+ brain) (Fig. 2D). In comparison, *Loa/+* embryos did not show any differences in Pax6 cell thickness nor total cell counts. There were also no significant differences in their distribution (Supplementary Fig. 2A-D).

During neurogenesis, intermediate progenitors (IPs) are generated from RG (Englund et al., 2005). Because of the changes in Pax6(+) cells, we correspondingly assessed Tbr2, a marker of IPs (Englund et al., 2005). We measured the Tbr2(+) subventricular zone (SVZ) thickness relative to cortical wall thickness in the developing somatosensory cortex (Fig. 2E-H). Labeled cells were located mainly in bins 1–3. In an

opposite trend to Pax6 labeling results, the SVZ represented 41% of the cortical wall in WT and 44.5% in L3/+ embryos, however for L2/+ embryos, this proportion was reduced to 37.2% (Fig. 2F). Tbr2(+) cell counts also changed significantly, reduced in L2/+ brains by 29% compared to WT, and also showing a 27% increase in L3/+ brains *vs* L2/+ (Fig. 2G). An abnormal Tbr2(+) cell distribution was also detected in L2/+ mutants (Fig. 2H). In WT and L3/+, bins 2 and 3 showed the main proportions of Tbr2(+) cells. In L2/+ mutants however, bin 2 showed the major distribution peak and there were significantly more IPs in bin 1 (26% L2/+ *vs* 20.3% WT) and less in bin 3 (26.3% L2/+ *vs* 33% WT). *Loa/+* brains showed no differences in number or distribution of Tbr2 cells with respect to WT (Supplementary Fig. 2E-H).

Thus in L2/+ mutants, Tbr2(+) cells show an opposite trend with respect to Pax6(+) cells, both in total counts and their distribution especially comparing bin 1 and bin 3. There appears to be a preferential production of Pax6(+) cells at the expense of Tbr2(+) cells at E14.5.

3.4. Apical descent of L2/+ RG nuclei may be altered

It is known that RG nuclei enter in S-phase in the basal part of the VZ and dynein plays a role in the apical descent of the nucleus towards the ventricular surface during G2, allowing cells to undergo mitosis (Tsai et al., 2010; Hu et al., 2013). As L2/+ brains showed less Pax6(+) cells in apical bins 1–2, and more in the basal bin 3, we further studied the phenomenon of INM, suspecting that in K3334N mutants this apical descent may be altered. To assess INM, BrdU injections were performed at E14.5, allowing incorporation of this thymidine analogue during S-phase, with sacrifice of animals performed at 0.5, 2 and 4 h later as schematized in Fig. 3A (Cappello et al., 2006). Anti-BrdU immunohistochemistry allowed us to identify the position of nuclei in the cortical wall and VZ over this period of time. In WT brains, we can expect that most BrdU-labeled nuclei after 0.5 and 2 h would localize in basal regions of the cortical VZ (*e.g.* mainly in bin 2), associated with the proportion of RG entering in S-phase (Fig. 3B-C). After 4 h in WT, the proportion of BrdU positive (+) nuclei appeared increased in bin 1 and decreased in bin 2 compared to 0.5 h, as nuclei descend to the apical surface. Thus, 62% of BrdU(+) nuclei in bin 2 after 0.5 h was reduced to 41% after 4 h, and 19% of BrdU(+) nuclei in bin 1 after 0.5 h was increased to 39% after 4 h. L3/+ nuclei showed a similar behavior suggesting that L3/+ RG perform INM as WT. However, L2/+ nuclei showed a notably higher proportion in bin 3 after 0.5 h than WT (31% L2/+ *vs* 16% WT), with less cells in bin 2 (45% L2/+ *vs* 62% WT) (Fig. 3B-C). Whereas WT and L3/+ showed a reduced proportion of BrdU(+) cells in bin 2 after 2 h compared to 0.5 h (WT: from 56% at 0.5 h to 42.7% at 2 h, L3/+: 68% to 47.4% at 2 h), this effect appeared

reduced for L2/+ (41% to 33% at 2 h). Finally, after 4 h in L2/+ the proportion of BrdU(+) nuclei was significantly lower than the WT in bin 1 (31% L2/+ *vs* 39% WT), and still higher in bin 3 (28% L2/+ *vs* 17% WT) suggesting that although an apical movement from basal to apical VZ occurred, L2/+ RG appear to exhibit a less efficient or delayed apical descent. Also, since values change little over time in bin 3, a proportion of L2/+ BrdU(+) nuclei may be blocked in the most basal part of the VZ. It is also notable that there appear to be more L2/+ BrdU(+) cells in bins 4–6 (after 0.5 and 2 h). Overall, these results might indicate a proportion of disorganized cycling progenitors, delayed or abnormal INM and/or an altered S phase progression.

To assess the specific impact of the K3334N mutation on these processes, we performed the same experiments using *Loa/+* animals (Supplementary Fig. 3A-B). We found that the BrdU(+) nuclei in this mutant exhibited INM, with the notable difference compared to WT that the proportion of *Loa/+* BrdU(+) nuclei after 4 h in the apical bin 1 was significantly higher (51.6% *Loa/+ vs* 39.3% WT) and significantly lower in bin 3 (7.9% *Loa/+ vs* 16.1% WT). This result has not been described previously and might suggest that *Loa/+* mutant RG nuclei move faster apically.

We also postulated that S-phase progression and potentially mitosis may be altered in L2/+ mutants. Indeed, because BrdU results suggest a less efficient apical descent of Pax6(+) nuclei we might expect ectopic or perturbed mitoses, and/or S-phase disruption. We hence set out to investigate further these cell cycle aspects.
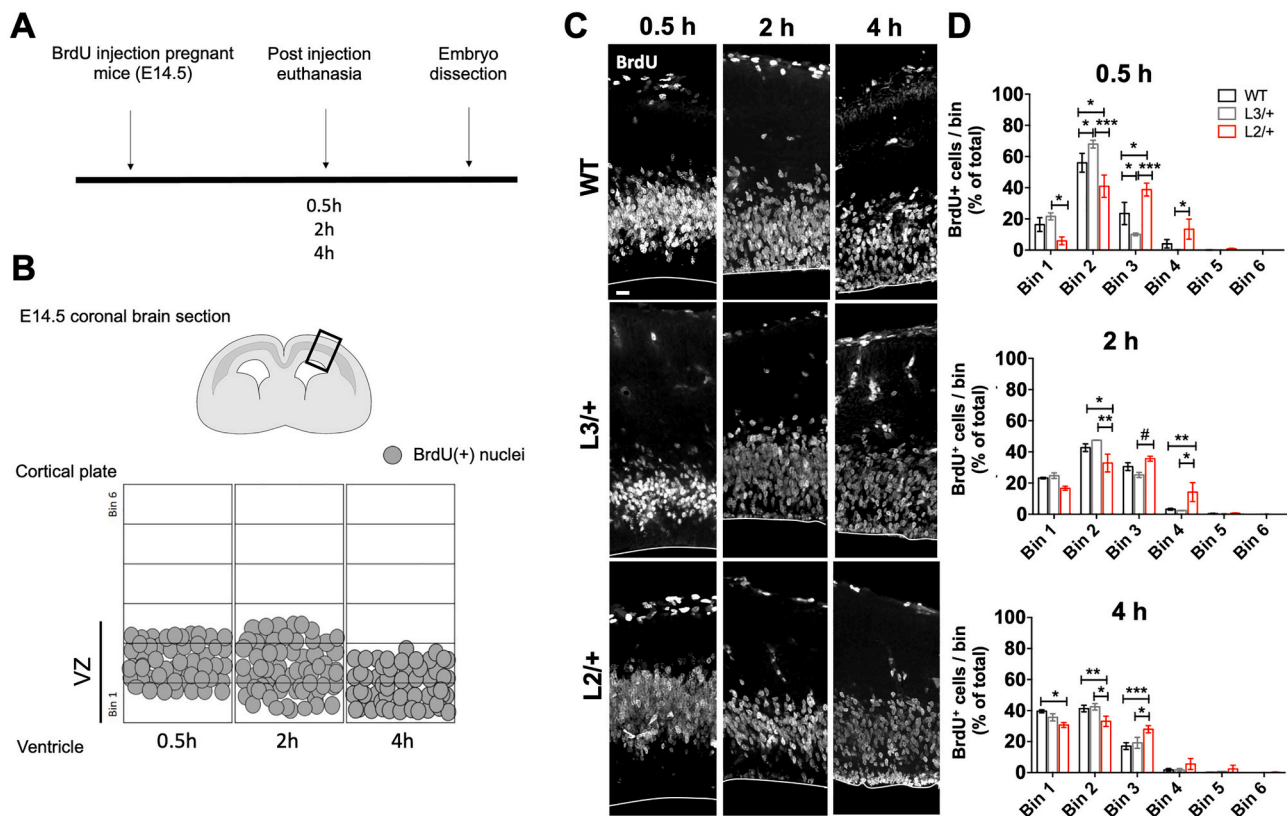

Fig. 3. INM is altered in L2/+ mouse brain. (A,B) Schemas showing the INM protocol (A) and nuclei localization in the cortical wall divided in 6 bins (B), after different BrdU injection times (0.5, 2 and 4 h). (C) Representative images of BrdU labeling on embryonic brain slices at E14.5 of WT, L3/+ and L2/+ genotypes. Freehand line in white represents the delimitation of the ventricular surface. Scale bar: 20 μm. (D) Quantification of BrdU+ nuclei distribution across the cortical wall expressed as % of total nuclei. Two-way ANOVA with *post hoc* Tukey's test was performed. 0.5 h: Interaction Bin x genotype, $F_{5,\ 40} = 85.8$, $p < 0.0001$ ($n = 4$ WT, $n = 4$ L3/+ and $n = 3$ L2/+ embryos). * $p < 0.041$, **** p < 0.0001. 2 h: Interaction Bin x genotype, $F_{5,\ 40} = 86.8$, $p < 0.0001$ ($n = 4$ WT, $n = 2$ L3/+ and $n = 4$ L2/+ embryos). * $p < 0.026$, ** $p < 0.009$. 4 h: Interaction Bin x genotype, $F_{5,\ 50} = 147.4$, $p < 0.0001$ ($n = 6$ WT, $n = 2$ L3/+ and $n = 4$ L2/+ embryos). * $p < 0.047$, ** $p < 0.007$, *** $p < 0.0003$.

3.5. RG cell cycle parameters are altered in L2/+ mice

We estimated the evolution of cells entering in S-phase between 0.5 h and 2 h after BrdU injections (Fig. 4A). In WT and L3/+, there was an increased proportion of cells entering in S phase at 2 h (26% and 34% respectively). However, in L2/+ animals this percentage was significantly lower (5%) compared to WT, suggesting reduced entry in S-phase, due to the K3334N mutation. In comparison, Loa/+ embryos did not exhibit significant differences in the proportion of S-phase entry compared to WT (Supplementary Fig. 4A).

Mitosis was then investigated in E14.5 brain sections. We observed no differences in the overall counts of phospho-histone positive (PH3+) cells (a marker for mitosis) between WT and L3/+ brains, although an increased trend was observed in L2/+ brains (32% increase) (Fig. 4B-C). In addition, PH3(+) cell distribution was altered in L2/+ embryos

compared to WT and L3/+ mice (Fig. 4D). Indeed, there were less mitotic cells apically in bin 1 (42% L2/+ vs 58% WT and 55% L3/+). Inversely, a significantly increased proportion of mitotic cells was revealed in basal regions, in bins 3–4 (22.6% L2/+ vs 12.6% L3/+ in bin 3, and 12.5% L2/+ vs 2.3% WT in bin 4). The alteration in mitotic cells is apparently specific to the K3334N mutation, since in Loa/+ brains, the F580Y mutation does not affect the total number of PH3+ cells and their distribution in the cortical wall (Supplementary Fig. 4B-D).

Proliferation index and cell cycle exit were next assessed using the cell proliferation marker Ki67 and BrdU labeling 24 h after injection. L2/+ and L3/+ mutant mice showed no significant differences in the proliferation index compared to WT (Fig. 4E-F). However, L2/+ proliferating cells showed an altered distribution along the cortical wall, with a decreased proportion in bin 2 (31.7% L2/+, 39.4% L3/+ and 37.8% WT) and an increased proportion in bin 3 (16.6% L2/+, 9.8% L3/+ and
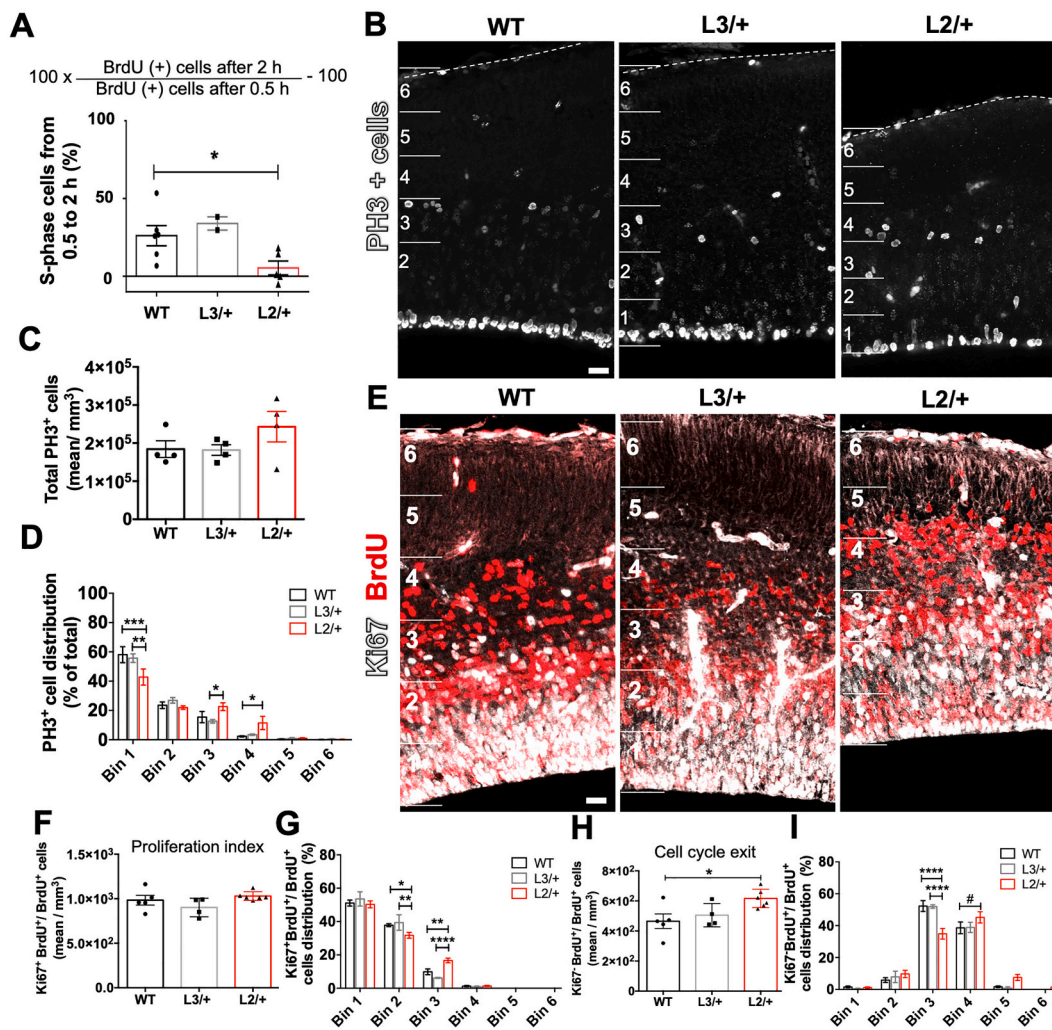

Fig. 4. Neuronal progenitors enter less in S-phase and mitotic cell distribution is altered in dynein K3334N mutant embryos. (A) Estimation of S-phase entry between 0.5 and 2 h expressed as %. Quantification of S phase entry in WT, L3/+, L2/+ brains expressed as %. Unpaired t-test, * $p = 0.0303$. (B) Representative immunolabelings of the mitotic marker PH3 in WT, L3/+ and L2/+ coronal brain sections at E14.5. Scale: 20 μm. (C) Quantifications of the number of PH3+ cells per volume (mm^3), mean ± SEM. One-way ANOVA with *post hoc* Tukey's test, $F_{2, 9} = 1.6$, n.s., $p = 0.26$ (n = 4 WT, n = 4 L3/+ and n = 4 L2/+ embryos). (D) Mitotic cell distribution across the cortical wall for WT, L3/+ and L2/+ embryos, mean ± SEM expressed as % of total. Two-way ANOVA with *post hoc* Tukey's test was performed. Interaction Bin x genotype, $F_{5, 45} = 142.7$, p < 0.0001 (n = 4 WT, n = 4 L3/+ and n = 4 L2/+ embryos). * $p < 0.045$, ** $p = 0.0028$, *** $p = 0.0004$. (E) Representative immunolabelings of the cell proliferation marker Ki67 and BrdU in WT, L3/+ and L2/+ coronal brain sections at E15.5. Scale: 20 μm. (F) Quantification of the proliferation index Ki67$^+$BrdU$^+$/BrdU$^+$ cells per volume (mm^3), mean ± SEM. One-way ANOVA with *post hoc* Tukey's test, $F_{2, 12} = 2.3$, n.s., $p = 0.14$ (n = 5 WT, n = 4 L3/+ and n = 6 L2/+ embryos). (G) Proliferating cell distribution across the cortical wall for WT, L3/+ and L2/+ embryos, mean ± SEM expressed as % of total. Two-way ANOVA with *post hoc* Tukey's test was performed. Interaction Bin x genotype, $F_{5, 72} = 569.3$, p < 0.0001 (n = 5 WT, n = 4 L3/+ and n = 6 L2/+ embryos). * $p < 0.016$, ** $p < 0.006$, **** $p = 0.0001$. (H) Quantification of cell cycle exit, Ki67$^-$BrdU$^+$/BrdU$^+$ cells per volume (mm^3), mean ± SEM. One-way ANOVA with *post hoc* Tukey's test, $F_{2, 12} = 4.9$, $p = 0.0028$; * $p < 0.028$. (I) Cell cycle exit distribution across the cortical wall, mean ± SEM expressed as % of total. Two-way ANOVA with *post hoc* Tukey's. Interaction Bin x genotype, $F_{5, 72} = 251.6$, p < 0.0001; **** p = 0.0001, # p = 0.09.

6.2% WT) (Fig. 4G). Interestingly, although the proliferation index was not changed significantly among genotypes, cell cycle exit was increased in L2/+ mice (32.6% increase in L2/+ *vs* WT) (Fig. 4H). In addition, non-proliferating BrdU labeled L2/+ cells were reduced in bin 3 (34.9% L2/+ *vs* 52.3% WT and 52% L3/+) with an opposite trend in bin 4 (Fig. 4I). These results might be in agreement with accumulating or blocked mitotic cells in more basal regions, impacting S-phase entry, and causing more cells to exit the cell cycle.

Loa/+ embryonic brains showed non-significant trends for reduced proliferation index (15%) and increased cell cycle exit (33%) (Supplementary Fig. 4E-F,H). No major differences in cell distribution were observed for *Loa/+* brains with the exception of an increased proportion of proliferating cells in bin 1 (62% Loa/+ *vs* 52% WT cells). These results are potentially coherent with the hypothesis of a faster apical descent increasing thus the proportion of proliferating cells in bin 1.

3.6. Increased cell death in L2/+ embryonic brains

Since microcephaly has been associated with increased cell death (Little and Dwyer, 2019), we analyzed apoptotic cell death in embryonic brain sections. The total number of active caspase-3(+) cells (a marker of apoptosis) across the cortical wall was significantly increased in L2/+ brains compared to WT (7.3 fold change) and to L3/+ (6.7 fold change) (Supplementary Fig. 5A-B). The majority of these apoptotic cells were localized in bins 1–3, suggesting that it is mainly progenitors that are susceptible to cell death when expressing the K3334N mutation. Apoptotic cells in *Loa/+* brains did not show significant differences compared to WT (Supplementary Fig. 5D-F). Coherently, increased apoptotic nuclei were also observed in L2/+ RG cell primary cultures compared to WT and L3/+ (Supplementary Fig. 5G-H), and apoptotic RG cells in Loa/+ were similar to WT cells (Supplementary Fig. 5I).
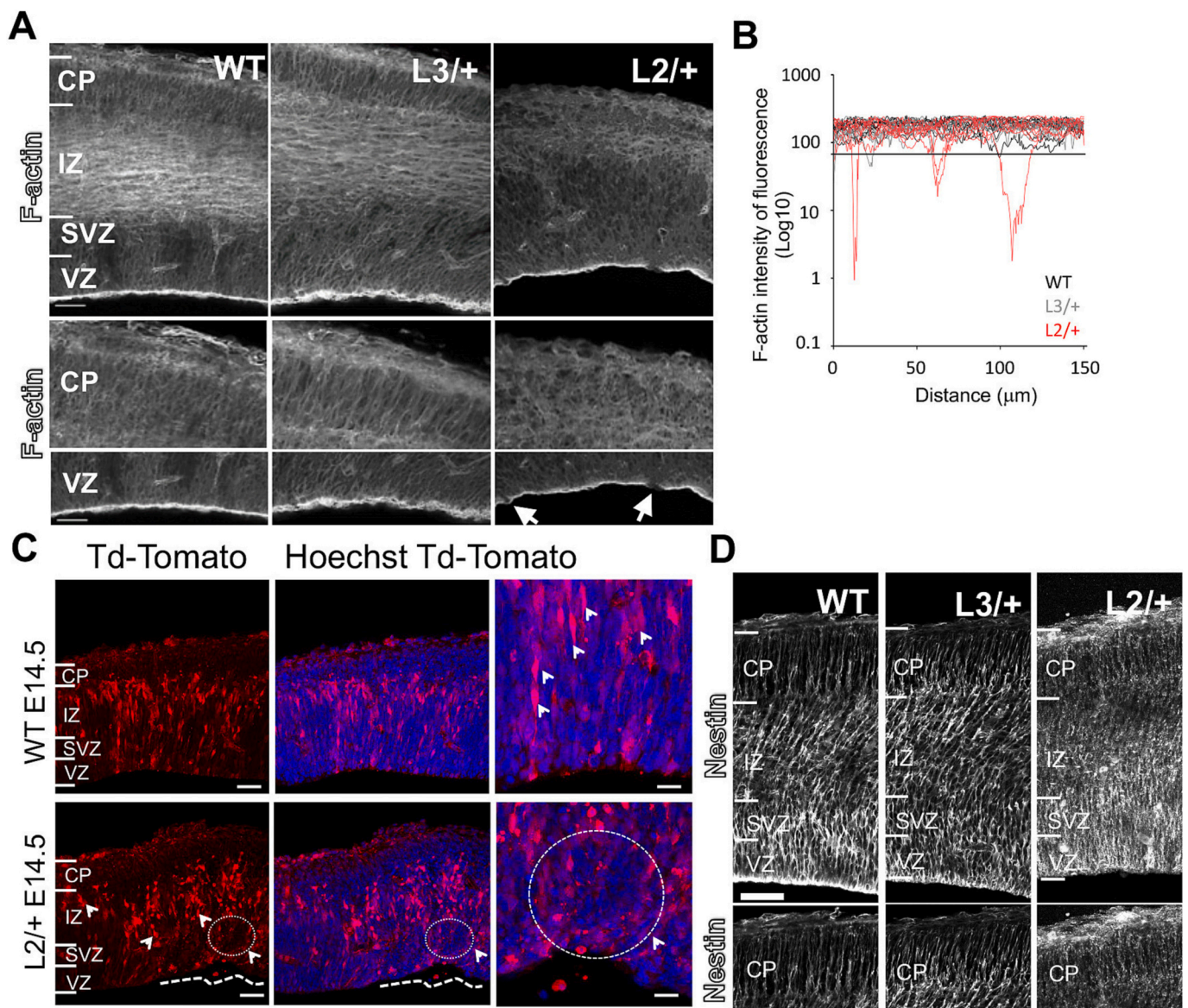

Fig. 5. The ventricular surface and RG scaffold are altered in K3334N mutants. (A) Representative images of F-actin staining in coronal brain sections at E14.5 (WT, L3/+ and L2/+). (B) Quantifications of F-actin labeling show periodic greatly reduced intensity in L2/+ brains suggesting fragmentation of the ventricular surface. (C) *In utero* electroporations at E14 showing 12 h later, Td-tomato positive cells with radial morphology in WT brains and a disrupted radial pattern in L2/+ brains. White arrows indicate radial morphology in WT and altered morphology in L2/+. Slashed line circle indicates a typical region of cells without radial morphology. Scale: 50 μm. (D) Representative images after staining for the intermediate filament nestin in E14.5 coronal brain sections (WT, L3/+ and L2/+). Note the perturbed pattern in L2/+ brains compared to WT and L3/+ (*e.g.* CP, cortical plate). Scale: 50 μm.

3.7. The ventricular surface and RG scaffold are altered in L2/+ mutants

Since the proportion of RG nuclei was reduced in the L2/+ apical VZ compared to WT, we wondered whether the ventricular surface might also be altered. F-actin, enriched in this region, was stained with phalloidin, revealing changes in the L2/+ ventricular boundary (Fig. 5A). The labeled ventricular surface notably appeared discontinuous: the fluorescence intensity of the phalloidin staining over 100 μm varied, approaching 0 at some points in L2/+ brains (Fig. 5B). This phenotype was not present in L3/+ embryos. In addition, F-actin staining showed an altered pattern across the cortical wall when L2/+ brains were compared to WT and L3/+ brains, especially noticeable in the cortical plate (CP), suggesting a less radial organization (Fig. 5A).

In utero electroporations (IUE) of CAG-Td-tomato at E14 helped reveal the normal RG morphology and radial distribution in WT brains, 12 h after electroporation. In L2/+ brains, the radial organization of RG appeared altered and often showed clusters of cells (Fig. 5C). Moreover, complementary immunolabelings with anti-nestin confirmed the RG defects in L2/+ brains (Fig. 5D), in which not only the nestin(+) fibers showed loss of radial organization, also the intensity of fluorescence appeared altered. This phenotype was observed with different severities in all L2/+ brains examined (n = 4). *Loa/+* brains did not show major defects in nestin fibers compared to WT (Supplementary Fig. 5J).

3.8. The K3334N mutation impairs proper neuronal migration

RG fiber organization was impaired in L2/+ cortices, which may suggest that neuronal migration could also be perturbed. In order to investigate this, we first analyzed the position of BrdU (+) cells at P0, 5 days after BrdU injection at E15 (Supplementary Fig. 6). Neurons born at E15 are destined for the upper cortical layers, which was their position in WT brains. In L2/+ brains, BrdU labeling was consistent with slowed or arrested migration, since the signal was more widely distributed, even across the deeper layers (see arrows, Supplementary Fig. 6).

We then looked more specifically at superficial neuron distribution within the cortical wall of P0 WT and L2/+ pups using immunolabelings of Satb2 (Britanova et al., 2008). A trend for a reduced number of Satb2 (+) neurons was observed in L2/+ brains compared to WT (15% reduction, Fig. 6B). In addition, Satb2 nuclei distribution was altered in L2/+ animals, showing a significantly increased proportion of Satb2(+) cells in deeper cortical regions (7.9 fold increase in bin 3 compared to the WT). There were also comparatively less Satb2(+) neurons in upper regions, notably bin 5 (21% less in L2/+ compared to WT) and bin 6 (28% less in L2/+ compared to WT) (Fig. 6A, C).

The fact that neurons are not present in their proper location in the CP strongly suggests that their migration is delayed, due to either a problem in the RG scaffolding, orientation of migration, and/or intrinsic defects in neurons themselves.

3.9. Subcellular impact of dynein mutations in neuronal progenitors in vitro

Dynein plays a key role in the intracellular transport of organelles (Pilling et al., 2006; Reck-Peterson et al., 2018). In addition, dynein is important to allow Golgi apparatus positioning in the cytoplasm (Harada et al., 1998; Marra et al., 2007; Reck-Peterson et al., 2018). We hence explored the impact of K3334N and F580Y missense mutations in primary cultures of Pax6(+) cells (Sun et al., 2011) on Golgi apparatus and mitochondria structural integrity, as well as their positioning.

First, we analyzed the peripheral membrane component of the cis-Golgi, using the GM130 antibody. L2/+ progenitors showed an expanded and elongated Golgi structure throughout the cytoplasm (Fig. 7A). There was also an increased volume of Golgi elements (L2/+ *vs* WT, 4 fold; L2/+ *vs* L3/+, 3.55 fold increase) (Fig. 7A-B). In addition, L2/+ cells showed an increased surface of Golgi elements (L2/+ *vs* WT, 3.1 fold; L2/+ *vs* L3/+, 2 fold increase) (Fig. 7C). Finally, their number per cell was increased in L2/+ compared to WT cells (L2/+ *vs* WT, 83% increase; L2/+ *vs* L3/+, 75% increase) (Fig. 7D).

Inverse results were observed for *Loa/+* cultures suggesting less expanded or elongated cis-Golgi structures compared to WT. *Loa/+* cells showed a reduced volume of Golgi elements (*Loa/+* *vs* WT, 11% decrease), with also a decreased surface (*Loa/+* *vs* WT, 12% decrease) and less spread compared to K3334N mutant cells (Supplementary Fig. 7A-D). The number of Golgi elements per cell was also decreased in *Loa/+* cells compared to WT (*Loa/+* *vs* WT, 35% decrease) (Supplementary Fig. 7A-D).

Mitochondrial morphology and length were also evaluated among L2 and L3 genotypes. L2/+ cells presented greatly disrupted mitochondrial networks compared to WT and L3/+ cultures. A reduced average mitochondrial length was found in L3/+ and L2/+ cells compared to WT (WT: 1.48 μm, L3/+: 1.1 μm and L2/+: 0.94 μm) (Fig. 7E). Mitochondrial morphology was also assessed. While tubular and intermediate forms, scored as 1 and 2 respectively, were the most common morphologies in WT progenitors, these were fewer in both L2/+ and L3/+
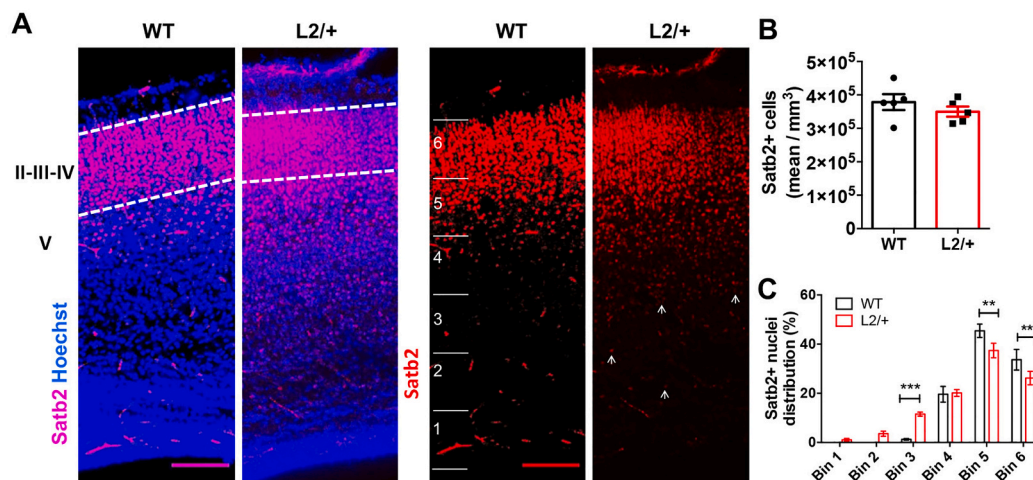

Fig. 6. Dynein K3334N mutation impairs proper neuronal migration. (A) Representative images of the upper layer neuronal marker Satb2 immunofluorescence and Hoechst staining (left) at P0 in WT and L2/+ brains. Satb2 immunofluorescence in coronal brain sections divided in 6 bins (right). Scale bar: 100 μm. (B) Quantification of cortical wall thickness of WT and L2/+ pup brains per volume (mm^3), mean ± SEM (n = 5 WT and n = 5 L2/+ embryos). Two-tailed unpaired t-test, n.s., $p = 0.34$. (C) Quantification of Satb2+ cell distribution across the cortical wall expressed as % of total. Two-way ANOVA with *post hoc* Bonferroni's test was performed. Interaction Bin x genotype, $F_{5, 24} = 75.11$, $p < 0.0001$ (n = 5 WT and n = 5 L2/+ embryos). ** $p < 0.0045$, *** p = 0.0001.
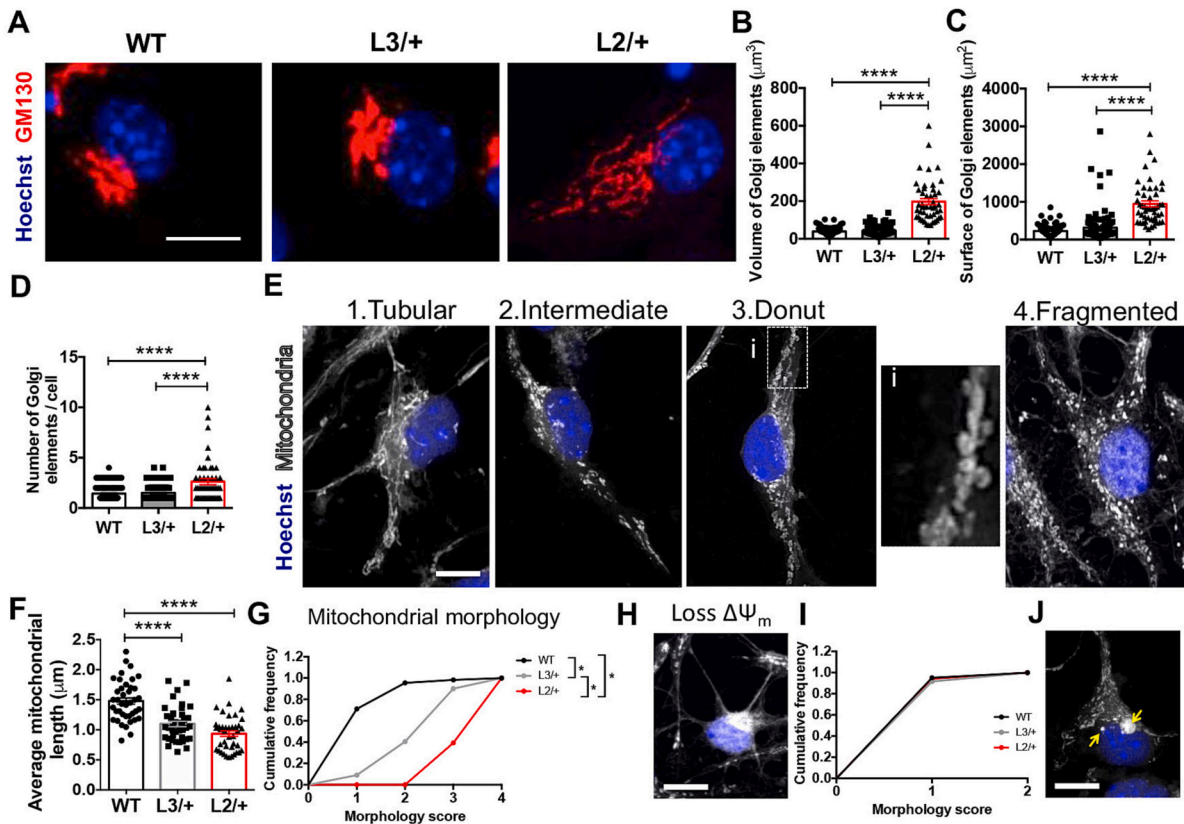
Fig. 7. L2/+ progenitor cells exhibit defects in Golgi apparatus and mitochondria morphology. (A) Representative immunolabelings of the cis-Golgi marker GM130 and Hoechst staining in WT, L3/+ and L2/+ Pax6 enriched primary cultures. Scale: 5 μm. (B) Quantification of Golgi elements volume (μm^3) among different genotypes. One-way ANOVA with *post hoc* Tukey's test, $F_{2, 254} = 180$, p < 0.0001 ($n = 103$ WT, $n = 106$ L3/+ and $n = 48$ L2/+ cells from 3 independent cell cultures); **** p < 0.0001. (C) Quantification of Golgi elements surface (μm^2) among different genotypes. One-way ANOVA with *post hoc* Tukey's test, $F_{2, 254} = 180$, p < 0.0001 (n = 103 WT, n = 106 L3/+ and n = 48 L2/+ cells from 3 independent cell cultures); **** p < 0.0001. (D) Quantification of Golgi elements per cell among different genotypes (mean ± SEM). One-way ANOVA with *post hoc* Tukey's test, $F_{2, 254} = 68.7$, p < 0.0001 (n = 103 WT, n = 106 L3/+ and n = 48 L2/+ cells from 3 independent cell cultures); **** p < 0.0001. (E) Representative images of MitoTracker Red labeling mitochondria and Hoechst staining of WT, L3/+ and L2/+ Pax6 enriched primary cultures. Micrographs show mitochondria with tubular, intermediate, donut-shaped and fragmented morphology. Scale: 5 μm. (F) Quantification of mitochondrial length in μm, expressed as mean ± SEM. One-way ANOVA with *post hoc* Tukey's test, $F_{2, 117} = 32.9$, p < 0.0001 (n = 40 WT, n = 40 L3/+ and n = 40 L2/+ cells from 3 independent cell cultures); **** p < 0.0001. (G) Analysis of mitochondrial morphology expressed as cumulative frequency of discreet categories (1: tubular, 2: intermediate, 3: donut, 4: fragmented mitochondria). Kruskal-Wallis followed by Dunn's *post hoc* test, p < 0.0001 ($n = 176$ WT, $n = 121$ L3/+ and $n = 112$ L2/+ cells from 3 independent cell cultures); **** p < 0.0001. (H) Representative micrograph of a cell with loss of $\Delta\Psi_m$. (I) Analysis of mitochondrial morphology expressed as cumulative frequency of discreet categories (1: mitochondria with $\Delta\Psi_m$, 2: mitochondria without $\Delta\Psi_m$). Kruskal-Wallis test, n.s., $p = 0.45$ ($n = 185$ WT, $n = 132$ L3/+ and $n = 119$ L2/+ cells from 3 independent cell cultures). (J) Representative micrograph of a cell with mitochondrial aggregates. Arrows indicate mitochondria aggregates. (For interpretation of the references to colour in this figure legend, the reader is referred to the web version of this article.)

cells (WT: 0.95, L3/+: 0.40 and L2/+: 0 cumulative frequencies). L2/+ cells in particular showed an increased proportion of donut-shaped and fragmented mitochondria, scored as 3 and 4 respectively (WT: 0.05, L3/+: 0.6 and L2/+: 1 cumulative frequencies) (Fig. 7F, G). Interestingly, the donut-shaped morphology, previously described associated with abnormal fusion events and partial mitochondrial detachment from the cytoskeleton under stress conditions (Liu and Hajnóczky, 2011), was not accompanied by an increased number of cells presenting mitochondrial membrane potential ($\Delta\Psi_m$) dissipation (Liu and Hajnóczky, 2011). Indeed, the loss of $\Delta\Psi_m$ was not changed among genotypes (Fig. 7H-I). Finally, mitochondria distribution in the cytoplasm did not seem to be perturbed in mutant conditions, although mitochondrial aggregates resembling mitoaggresomes (Lee et al., 2010; Vives-Bauza et al., 2010; Eschbach et al., 2013) were occasionally detected in L3/+ and L2/+ mutant conditions (Fig. 7J).

In order to further examine the impact of the K3334N mutation on mitochondrial morphology, we conducted electron microscopy (EM) studies in primary cultures of cortical Pax6(+) cells. Although total numbers of mitochondria did not change (Supplementary Fig. 8A-B), a proportion of cells presented altered mitochondrial morphology,

including swelling and vacuolization in the L3/+ mutant (25/25 cells) compared to WT (4/25 cells analyzed) (Supplementary Fig. 8A,C). Mitochondria with vacuolization presented an expansion of the intermembrane space (asterisk) and intermembrane remnants (arrowhead). In addition, donut morphology was also detected (Supplementary Fig. 8A-D). Indeed, a significant increase of mitochondrial vacuolization with a central space when transversally sectioned are represented as donut-shape mitochondria (arrows). Finally, large aggregates of non-altered mitochondria in autophagic vacuoles (two arrows) were also detected in L3/+ mutant cells (Supplementary Fig. 8A). These findings were consistent with the observed intense MitoTracker labeling resembling mitochondrial aggregates or mitoaggresomes (Fig. 7I).

Thus, the dynein K3334N mutation revealed organelle structural alterations in progenitor cell cultures, which may be caused by a pathological disruption of microtubule transport and dynein-interacting partners mediating cargo transport.

4. Discussion

In this study we characterized the impact of the *Dync1h1* K3334N

mutation on mouse corticogenesis. We focused mainly on RG progenitors, since the role of dynein has been well-characterized in these cells and defects might explain subsequent brain development alterations observed in Human. This is the first mouse model characterized for a *de novo DYNC1H1* patient mutation associated with a cortical malformation (Poirier et al., 2013).

Although studies on human *DYNC1H1* mutations associated with SMA-LED have been performed previously (Harms et al., 2012), the p. Lys3336Arg mutation studied here is associated predominantly with microcephaly with a complex cortical malformation (Poirier et al., 2013). The brain phenotype of the K3334N mutant mouse mimics these features, exhibiting severe cortical defects such as reduced brain size starting during embryogenesis and continuing postnatally. Pax6(+) cells were increased and Tbr2(+) cells were reduced and abnormally distributed throughout the cortical wall, as were mitotic and proliferative cells. INM appears perturbed with proportionally less cells descending apically during the time period analyzed. In addition, there is increased cell death among progenitor types. The ventricular surface of embryonic brains is discontinuous and RG radiality is disrupted. Furthermore, organelles are affected in Pax6(+) cells in culture, with the Golgi apparatus and mitochondria showing subcellular alterations in their structural integrity. As well as progenitor defects, neuronal migration, particularly studied for upper layer neurons, appears less efficient compared to WT brains. These data shed light on microcephaly and dysgyria features of the human phenotype. Interestingly as well, the heterozygote mouse mutant also exhibits a smaller body, walks with an unusual gait and shows reduced survival after 3 weeks. Thus, the mutant mouse is particularly severely affected, revealing more than just a brain phenotype.

L2/+ mice die after several weeks of life. To study the effects of this mutation, it was necessary to produce L2/+ mutants by directly crossing L3/+ with pActb-Flpe deleter mice to remove the neo cassette in each new generation, this procedure also being recommended to avoid confounding neo cassette artifacts. Interestingly, L3/+ mice appear to show reduced quantities of mutant alleles, although total transcripts appear unaltered in quantity (Supplementary information and Supplementary Fig. 1). Hybrid transcripts were observed incorporating the neo cassette, although it is unclear how stable these are. Overall, in these mice Dync1h1 protein levels appear unchanged compared to WT, potentially due to compensation by the WT allele. These results may explain why L3/+ mice appear largely as WT, although there is also room for some phenotypes to emerge potentially due to small amounts of an altered protein containing both the missense mutation and the neo cassette. Western blot data suggest on the other hand, that Dync1h1 expression is reduced in L2/+ progenitor cells. This may be because of instability of the mutant protein or transcript (in the absence of the neo cassette), leading to its degradation, without major compensation by the WT allele. Dync1h1 protein dosage is clearly critical for correct cortical development. In fact, in a *Dync1h1* KO mouse model, no embryos were observed after E8.5 (Harada et al., 1998). Thus, subtle modifications of Dync1h1 quantities, due to a cortical malformation missense mutation, have a severe effect on cortical development.

4.1. Subtle cortical development defects in the Loa/+ model

To better clarify the specific impact of this mutation on mouse brain development we compared several of our results with a well-characterized mouse model (*Loa/+*) associated with peripheral neuropathies. The *Loa* model was not known previously to exhibit cortical development defects in the heterozygous state (Ori-McKenney and Vallee, 2011). Also, little was known and previously studied concerning its impact on cortical progenitors. Overall, we identified few differences in this model compared to WT. Nevertheless, in our detailed progenitor analyses, we were able to show a potentially increased apical descent of nuclei during INM and increased number of proliferating cells in the most apical region (bin 1). Interestingly as well, a trend for increased cell

cycle exit was observed in *Loa/+* brains. Moreover, cis-Golgi morphology was altered in *Loa/+* mutant progenitor cells. These data suggest that subtle brain alterations cannot be ruled out in heterozygote mouse brains, and potentially even when considering SMA-LED-like mutations in human. Indeed, it has now become apparent that patients may have broader clinical spectrums than previously thought, with a number of patients exhibiting both cortical malformations and SMA-LED symptoms (Becker et al., 2020). In addition, although many SMA-LED mutations have previously been associated with the tail domain of DYNC1H1 and inversely many cortical malformation mutations with the motor domain, their impact on the function of these domains and also with respect to different organs, is clearly not yet well understood. Some SMA-LED and cortical malformation mutations also fall in opposing protein domains (Schiavo et al., 2013). Further analyses are required to finely dissect the impacts of individual mutations on DYNC1H1 functions.

4.2. The role of dynein in neuronal progenitor INM and cell cycle

Dynein plays an important role pulling cargos such as the RG nucleus and membrane-bound organelles, along microtubule tracks (Tolić-Nørrelykke, 2008; Taverna and Huttner, 2010). In addition, since the K3336N mutation located in the MTBD strongly affects the dynein-dynactin-BICD2N complex (Hoang et al., 2017), we studied whether this mutation could impact in RG function and have consequences during cortical development. Particularly, during INM, we identified defects focused on the apical movement of RG nuclei from the basal VZ in S/G2 phases to the ventricular surface where cells undergo mitosis. Our results suggest that dynein mutations (and potentially dynein dosage) affect this apical movement. Interestingly, in *Loa/+* progenitor cells there is a tendency for increased dynein/BicD2 expression (three times more) and we observed an increased number of BrdU(+) nuclei in apical regions after 4 h compared to WT, which may suggest a faster apical movement between 2 and 4 h. Inversely, L2/+ progenitors had apparently decreased Dync1h1 and reduced BicD2 and exhibited slower/less apical movement suggested by a decreased percentage of BrdU(+) cells apically after 4 h of BrdU injection. Interestingly, Hoang et al. (2017) also showed that K3336N DYNC1H1 colocalization with BICD2N was decreased to ≈50%. Alternative explanations for our INM results involve the significantly greater proportion of L2/+ BrdU(+) cells present at each time point in bin 3 compared to WT and L3/+. Might these be blocked or apoptotic cells, effectively therefore reducing the proportion of cells descending apically? Our results suggest that these are unlikely to be Tbr2(+) cells, since fewer are observed in bin 3 in the mutant. It is however interesting that these cells are revealed even 0.5 h after having taken up BrdU, and proliferation index is also increased in bin 3. An increased proportion of mitotic cells is similarly present in bin 3. Cells appear to remain blocked in this bin and this may effectively deplete the RG progenitor pool of nuclei able to descend to the ventricular surface. In addition, since the VZ relative depth is increased in L2/+ embryos, it is possible that apical descent is less efficient during the time period analyzed because nuclei may have to descend a greater distance than WT.

Of note, previous *in vitro* studies have shown that recombinant dynein expression was not altered by the presence of the K3336N mutation in insect cells using the baculovirus system (Hoang et al., 2017). The mutation appeared though to reduce the frequency of dynein movements and to alter the capacity of this subunit to associate with certain of its protein partners including dynactin and BICD2 (Hoang et al., 2017). The run length and velocity of the dynein-dynactin-BICD2 (DDB) complex was reduced under these conditions. Perturbed functions of the DDB complex detected *in vitro* related to the K3336N mutation could help explain several of the phenotypes observed in the KI mouse model. For the *Loa* F580Y missense mutation, only run length of the DDB complex was reduced, with binding of dynein to its partners not altered. In addition though, this tail mutation was shown to exhibit increased

microtubule gliding velocity (Hoang et al., 2017). This could be in agreement with our results suggesting a faster apical nuclear movement of *Loa/+* progenitors.

Importantly, it is of much interest how INM may regulate cell cycle progression of RG and *vice versa*. For example, cytochalasin B is known to inhibit apical nuclear movement and cause ectopic (basal) mitoses (Karfunkel, 1972; Murciano et al., 2002). The interpretation is that mitosis still occurs but at the position where the nuclei were trapped. Concerning our data, it is thus possible that because apical movement is less efficient, cells also undergo mitosis basally. It is also possible that less apical movement could be due to the fact that fewer cells enter in S-phase in L2/+ embryos and hence there are fewer cells available to descend. But how INM progression impacts S-phase progression is still not fully elucidated. Another explanation for the overall unaffected proliferation index could be due to a mitotic lengthening/delay. Thus, there are several potential explanations to account for both less descending nuclei to the ventricular surface, as well as increased Pax6 (+) cells in bin 3. Also, cell differentiation (*e.g.* cell cycle exit) and the lengthening of the cell cycle have been well documented in different stem cell lineages (Lange and Calegari, 2010). It has been shown that longer mitosis of RG progenitors directly alters neuronal fate specification and progeny viability, which can be associated with microcephaly (Pilaz et al., 2016; Mitchell-Dick et al., 2020). Therefore, this would be in agreement with our results, in which L2/+ progenitors show not only a reduced S-phase entry, but also trends for higher numbers of proliferating cells (*e.g.* Ki67, PH3), potentially due to mitotic lengthening, which may encourage cell cycle exit (Calegari et al., 2005).

4.3. Neurogenesis and neuron organization alterations

Our results suggest that neuronal migration is impaired/delayed and the layer specific positioning of Satb2(+) neurons is reduced at P0. Of note, Satb2(+) neurons are produced in large majority from E14.5 to E15.5 (Britanova et al., 2006). Also, we observed that RG fibers are misoriented at mid-corticogenesis and this could strongly contribute to these phenotypes. These data together may suggest that the RG cannot act as a proper support for neuronal migration but also generation of neurons from reduced IPs may not be performed at the proper location, these non-cell autonomous effects influencing migration. In addition, if neurogenesis was impaired before E14.5, because of RG over-proliferation as evidenced by increased Pax6+ cells, this could contribute to impacts on neuronal layer formation. The combined phenotypes may explain the upper layer neuron distribution alterations observed.

It has been shown that defects during neuronal migration in BicD2 deficient mice affect the later born upper layer neurons (Will et al., 2019), similar to the results shown in our study. A recent study concerning a new *BICD2* mutation in a cortical malformation patient also showed that it affects neuronal migration (Tsai et al., 2020). BicD2 is involved in dynein recruitment at the nuclear envelope, an essential step for neuronal migration (Vallee et al., 2009; Bertipaglia et al., 2018), and the BICD2 cortical malformation patient mutation affects its localization, as well as dynein's, at the nuclear envelope, when studied in the mouse. Interestingly, when BicD2 carries a SMA-LED patient mutation, both proteins are well localized at the nuclear envelope (Tsai et al., 2020), potentially suggesting that nuclear envelope dynein recruitment defects are a specific feature of cortical malformation disorders.

4.4. Specific subcellular alterations due to Dync1h1 mutation

Organelles, such as mitochondria and the Golgi apparatus, need the interaction from the pulling forces elicited by the dynein complex and its regulators, for their appropriate positioning and function (Jaarsma and Hoogenraad, 2015; Reck-Peterson et al., 2018). Defects in the structural integrity of several organelles as well as their subcellular localization have been described in other models presenting mutations in *Dync1h1*

(Harada et al., 1998; Eschbach et al., 2013). Harada et al. (1998) showed that cells from the blastocyst of KO mice, from which embryos do not survive beyond this stage, exhibited a highly vesiculated Golgi apparatus, as well as endosomes and lysosomes which were abnormally distributed throughout the cytoplasm. These results are consistent with what we observed in L2/+ progenitor cultures, particularly showing more dispersion, with an increased volume, surface and number of cis-Golgi elements, and pointing potentially to the mutation site as being a relevant target for these cargo interactions. These defects could be also due to the reduction of Dync1h1 levels in the L2/+ RG primary cultures. It is interesting to highlight the question of whether different Dync1h1 regulators and adaptors might be differentially affected depending upon the mutant conditions, and thus some organelle-specific transports, which might be identified in the future.

We also show altered mitochondrial morphology, including reduced length, increased fragmentation and the striking donut-like shape. An increased fragmentation and functional defects were previously reported by Eschbach et al. (2013), in mouse embryonic fibroblasts containing a point mutation in *Dync1h1* (*Cramping* allele of the *Dync1h1*, p. Y1055C mutation) and in patient fibroblasts with SMA-LED mutations. These authors also reported mitochondrial aggregates as were occasionally observed in mutant RG progenitors. Moreover, we show that K3334N Pax6(+) cells presented increased donut-like shapes, which were also demonstrated by EM and have previously been associated with hypoxia-reoxygenation impaired mitochondria dynamics (Liu and Hajnóczky, 2011). The donut-like shape is triggered by the opening of the permeability transition pore or K+ channels, causing mitochondrial swelling and partial detachment from the cytoskeleton which finally favours anomalous fusion events, such as autofusion and fusion at several sites among 2–3 mitochondria, ending in the characteristic donuts and a progressive loss of mitochondrial Drp1-independent fusion activity (Liu and Hajnóczky, 2011). We can speculate that this abnormal morphology observed in the K3334N mutant affecting the motor domain, could be related similarly to a partial detachment of the dynein-cargo complex from microtubules. Interestingly, it was shown that mitochondria fusion-fission dynamics could influence post mitotic cell fate in a restricted window of time (Iwata et al., 2020), and this could potentially be related to microcephaly in the patient and K3334N mutant mice. In addition, we cannot exclude a fusion-fission imbalance and further metabolic defects in mutants such as reported by Eschbach et al. (2013). The importance of cell metabolism in the proliferative capacity of cortical progenitors, brain expansion and evolution has recently been well documented (Gkini and Namba, 2022). Finally, Iwata et al. (2023) demonstrated that pharmacological or genetic manipulation of developing cortical neurons could modify mitochondrial metabolism allowing changes in their differentiation, maturation and synapse formation. The implication of dynein mutations in mitochondrial morphology and metabolism together with a potential crosstalk with neurodegenerative phenomena, will be interesting topics to pursue in the future.

5. Conclusions

In this study we provide the characterization of a new dynein KI mutant mouse which has phenotypical features mimicking certain aspects of the brains of cortical malformation patients exhibiting dynein mutations (*e.g.* K3336N). The impact of this missense mutation on progenitors was observed at cellular and subcellular levels, contributing to a better understanding of Dync1h1-related patho-mechanisms during cortical development. Notably RG and IP numbers and localization were disturbed, as well as defective INM and cell cycle parameters in progenitors. Also, increased cell death and defects in RG fibers and radial organization can help explain the smaller brain and neuronal migration defects observed postnatally. The integrity of key organelles was also perturbed (e.g mitochondria and Golgi) in RG. Of note, fewer defects were observed in a SMA-LED-like mouse model (*Loa)* although some

alterations were observable in progenitors during cortical development. The K3334N mouse model also exhibited body development defects. Therefore, we present here a new and relevant mouse model to study Dync1h1 impact on cortical development.

Supplementary data to this article can be found online at https://doi.org/10.1016/j.nbd.2023.106085.

Funding

CRediT authorship contribution statement

Delfina M. Romero: Conceptualization, Validation, Writing – original draft, Writing – review & editing, Formal analysis, Investigation, Visualization, Supervision. **Donia Zaidi:** Conceptualization, Validation, Writing – original draft, Writing – review & editing, Formal analysis, Investigation, Visualization. **Carmen Cifuentes-Diaz:** Investigation. **Camille Maillard:** Methodology, Validation, Formal analysis. **Gael Grannec:** Investigation, Formal analysis. **Mohammed Selloum:** Methodology, Investigation, Formal analysis. **Marie-Christine Birling:** Methodology, Investigation, Formal analysis. **Nadia Bahi-Buisson:** Conceptualization, Project administration, Funding acquisition, Resources. **Fiona Francis:** Conceptualization, Writing – original draft, Writing – review & editing, Project administration, Funding acquisition, Resources, Visualization, Supervision.

Declaration of Competing Interest

The authors have no competing interests.

Data availability

Data will be made available on request.

Acknowledgements

References

Becker, L.L., et al., 2020. The clinical-phenotype continuum in DYNC1H1-related disorders—genomic profiling and proposal for a novel classification. J. Hum. Genet. 65 (11) https://doi.org/10.1038/s10038-020-0803-1.

Bertipaglia, C., et al., 2018. Nuclear migration in mammalian brain development. Semin. Cell Dev. Biol. 82. https://doi.org/10.1016/j.semcdb.2017.11.033.

Birling, M.C., Dierich, A., Jacquot, S., et al., 2012. Highly-efficient, fluorescent, locus directed cre and FlpO deleter mice on a pure C57BL/6N genetic background. Genesis 50 (6). https://doi.org/10.1002/dvg.20826.

Bizzotto, S., Francis, F., 2015. Morphological and functional aspects of progenitors perturbed in cortical malformations. Front. Cell. Neurosci. 9 (FEB) https://doi.org/10.3389/fncel.2015.00030.

Bolhy, S., et al., 2011. A Nup133-dependent NPC-anchored network tethers centrosomes to the nuclear envelope in prophase. J. Cell Biol. 192 (5) https://doi.org/10.1083/jcb.201007118.

Borrell, V., Götz, M., 2014. Role of radial glial cells in cerebral cortex folding. Curr. Opin. Neurobiol. 27. https://doi.org/10.1016/j.conb.2014.02.007.

Britanova, O., et al., 2006. A novel mode of tangential migration of cortical projection neurons. Dev. Biol. 298 (1). https://doi.org/10.1016/j.ydbio.2006.06.040.

Britanova, O., et al., 2008. Satb2 is a Postmitotic determinant for upper-layer neuron specification in the neocortex. Neuron 57 (3). https://doi.org/10.1016/j.neuron.2007.12.028.

Calegari, F., et al., 2005. Selective lengthening of the cell cycle in the neurogenic subpopulation of neural progenitor cells during mouse brain development. J. Neurosci. 25 (28). https://doi.org/10.1523/JNEUROSCI.0778-05.2005.

Cappello, S., et al., 2006. The rho-GTPase Cdc42 regulates neural progenitor fate at the apical surface. Nat. Neurosci. 9 (9) https://doi.org/10.1038/nn1744.

Di Pizio, A., et al., 2023. A conditional null allele of Dync1h1 enables targeted analyses of dynein roles in neuronal length sensing. J. Cell Sci. 136 (5) https://doi.org/10.1242/jcs.260220.

El-Kadi, A.M., et al., 2010. The legs at odd angles (Loa) mutation in cytoplasmic dynein ameliorates mitochondrial function in SOD1G93A mouse model for motor neuron disease. J. Biol. Chem. 285 (24) https://doi.org/10.1074/jbc.M110.129320.

Englund, C., et al., 2005. Pax6, Tbr2, and Tbr1 are expressed sequentially by radial glia, intermediate progenitor cells, and Postmitotic neurons in developing neocortex. J. Neurosci. 25 (1) https://doi.org/10.1523/JNEUROSCI.2899-04.2005.

Eschbach, J., et al., 2013. Dynein mutations associated with hereditary motor neuropathies impair mitochondrial morphology and function with age. Neurobiol. Dis. 58. https://doi.org/10.1016/j.nbd.2013.05.015.

Frith, C., 1996. The role of the prefrontal cortex in self-consciousness: the case of auditory hallucinations. Philos. Transact. Roy. Soc. B: Biol. Sci. *351* (1346) https://doi.org/10.1098/rstb.1996.0136.

Gacem, N., et al., 2020. ADAR1 mediated regulation of neural crest derived melanocytes and Schwann cell development. Nat. Commun. 198 (11) https://doi.org/10.1038/s41467-019-14090-5.

Garrett, C.A., et al., 2014. DYNC1H1 mutation alters transport kinetics and ERK1/2-cFos signalling in a mouse model of distal spinal muscular atrophy. Brain 137 (7), 1883–1893. https://doi.org/10.1093/brain/awu097.

Gkini, V., Namba, T., 2022. Glutaminolysis and the control of neural progenitors in neocortical development and evolution. Neuroscientist. 20 https://doi.org/10.1177/10738584211069060.

Götz, M., et al., 1998. Pax6 controls radial glia differentiation in the cerebral cortex. Neuron 21 (5). https://doi.org/10.1016/S0896-6273(00)80621-2.

Harada, A., et al., 1998. Golgi Vesiculation and lysosome dispersion in cells lacking cytoplasmic dynein. J. Cell Biol. 141 (1) https://doi.org/10.1083/jcb.141.1.51.

Harms, M.B., et al., 2012. Mutations in the tail domain of DYNC1H1 cause dominant spinal muscular atrophy. Neurology 78 (22). https://doi.org/10.1212/WNL.0b013e3182556c05.

He, Y., et al., 2005. Role of cytoplasmic dynein in the axonal transport of microtubules and neurofilaments. J. Cell Biol. 168 (5). https://doi.org/10.1083/jcb.200407191.

Hoang, H.T., et al., 2017. DYNC1H1 mutations associated with neurological diseases compromise processivity of Dynein-Dynactin-Cargo adaptor complexes. Proc. Natl. Acad. Sci. U. S. A. 114 (9) https://doi.org/10.1073/pnas.1620141114.

Hu, D.J.K., et al., 2013. Dynein recruitment to nuclear pores activates apical nuclear migration and mitotic entry in brain progenitor cells. Cell 154 (6). https://doi.org/10.1016/j.cell.2013.08.024.

Ilieva, H.S., et al., 2008. Mutant Dynein (Loa) triggers proprioceptive axon loss that extends survival only in the SOD1 ALS model with highest motor neuron death. Proc. Natl. Acad. Sci. U. S. A. 105 (34) https://doi.org/10.1073/pnas.0805422105.

Iwata, R., et al., 2020. Mitochondrial dynamics in postmitotic cells regulate neurogenesis. Science 369 (6505). https://doi.org/10.1126/science.aba9760.

Iwata, R., et al., 2023. Mitochondria metabolism sets the species-specific tempo of neuronal development. Science 379 (6632). https://doi.org/10.1126/science.abn4705 eabn4705.

Jaarsma, D., Hoogenraad, C.C., 2015. Cytoplasmic dynein and its regulatory proteins in golgi pathology in nervous system disorders. Front. Neurosci. 9 (OCT) https://doi.org/10.3389/fnins.2015.00397.

Karfunkel, P., 1972. The activity of microtubules and microfilaments in neurulation in the Chick. J. Exp. Zool. 181 (3) https://doi.org/10.1002/jez.1401810302.

Lange, C., Calegari, F., 2010. Cdks and cyclins link G1 length and differentiation of embryonic, neural and hematopoietic stem cells. Cell Cycle 9 (10). https://doi.org/10.4161/cc.9.10.11598.

Lee, H.Y., et al., 2010. Targeted expression of catalase to mitochondria prevents age-associated reductions in mitochondrial function and insulin resistance. Cell Metab. 12 (6). https://doi.org/10.1016/j.cmet.2010.11.004.

Little, J.N., Dwyer, N.D., 2019. P53 deletion rescues lethal microcephaly in a mouse model with neural stem cell abscission defects. Hum. Mol. Genet. 28 (3) https://doi.org/10.1093/hmg/ddy350.

Liu, X., Hajnóczky, G., 2011. Altered fusion dynamics underlie unique morphological changes in mitochondria during hypoxia-reoxygenation stress. Cell Death Differ. 18 (10) https://doi.org/10.1038/cdd.2011.13.

Marra, P., et al., 2007. The biogenesis of the Golgi ribbon: the roles of membrane input from the ER and of GM130. Mol. Biol. Cell 18 (5). https://doi.org/10.1091/mbc. E06-10-0886.

Mitchell-Dick, A., et al., 2020. Acute lengthening of progenitor mitosis influences progeny fate during cortical development in vivo. Dev. Neurosci. https://doi.org/10.1159/000507113.

Mizuno, N., et al., 2007. Three-dimensional structure of cytoplasmic dynein bound to microtubules. Proc. Natl. Acad. Sci. U. S. A. 104 (52) https://doi.org/10.1073/pnas.0710406105.

Murciano, A., et al., 2002. Interkinetic nuclear movement may provide spatial clues to the regulation of neurogenesis. Mol. Cell. Neurosci. 21 (2) https://doi.org/10.1006/mcne.2002.1174.

Ori-McKenney, K.M., Vallee, R.B., 2011. Neuronal migration defects in the Loa dynein mutant mouse. Neural Dev. 6 (1) https://doi.org/10.1186/1749-8104-6-26.

Palade, G.E., 1952. A study of fixation for electron microscopy. J. Exp. Med. 95 (3) https://doi.org/10.1084/jem.95.3.285.

Palmer, T.D., et al., 2000. Vascular niche for adult hippocampal neurogenesis. J. Comp. Neurol 425 (4). https://doi.org/10.1002/1096-9861(20001002)425:4<479::aid-cne2>3.0.co;2-3.

Parrini, E., et al., 2016. Genetic basis of brain malformations. Mol. Syndromol. 7 (4) https://doi.org/10.1159/000448639.

Paschal, B.M., Vallee, R.B., 1987. Retrograde transport by the microtubule-associated protein MAP 1C. Nature 330 (6144) https://doi.org/10.1038/330181a0.

Pilaz, L.J., et al., 2016. Prolonged mitosis of neural progenitors alters cell fate in the developing brain. Neuron 89 (1). https://doi.org/10.1016/j.neuron.2015.12.007.

Pilling, A.D., et al., 2006. Kinesin-1 and dynein are the primary motors for fast transport of mitochondria in Drosophila motor axons. Mol. Biol. Cell 17 (4). https://doi.org/10.1091/mbc.E05-06-0526.

Poirier, K., et al., 2013. Mutations in TUBG1, DYNC1H1, KIF5C and KIF2A cause malformations of cortical development and microcephaly. Nat. Genet. 45 (6), 639–647. https://doi.org/10.1038/ng.2613.

Rakic, P., 1972. Mode of cell migration to the superficial layers of fetal monkey neocortex. J. Comp. Neurol. 145 (1) https://doi.org/10.1002/cne.901450105.

Rakic, P., et al., 2009. Decision by division: making cortical maps. Trends Neurosci. 32 (5) https://doi.org/10.1016/j.tins.2009.01.007.

Reck-Peterson, S.L., et al., 2018. The cytoplasmic dynein transport machinery and its many cargoes. Nat. Rev. Mol. Cell Biol. 19 (6) https://doi.org/10.1038/s41580-018-0004-3.

Rodríguez, C.I., et al., 2000. High-efficiency deleter mice show that FLPe is an alternative to Cre- LoxP. Nat. Genet. 25 (2) https://doi.org/10.1038/75973.

Romero, D.M., et al., 2018. Genetics and mechanisms leading to human cortical malformations. Semin. Cell Dev. Biol. 76. https://doi.org/10.1016/j.semcdb.2017.09.031.

Schiavo, G., et al., 2013. Cytoplasmic dynein heavy chain: the servant of many masters. Trends Neurosci. 36 (11) https://doi.org/10.1016/j.tins.2013.08.001.

Spear, P.C., Erickson, C.A., 2012. Interkinetic nuclear migration: a mysterious process in search of a function. Develop. Growth Differ. 54 (3). https://doi.org/10.1111/j.1440-169X.2012.01342.x.

Splinter, D., et al., 2010. Bicaudal D2, dynein, and Kinesin-1 associate with nuclear pore complexes and regulate centrosome and nuclear positioning during mitotic entry. PLoS Biol. 8 (4) https://doi.org/10.1371/journal.pbio.1000350.

Splinter, D., et al., 2012. BICD2, dynactin, and LIS1 cooperate in regulating dynein recruitment to cellular structures. Mol. Biol. Cell 23 (21). https://doi.org/10.1091/mbc.E12-03-0210.

Subramanian, L., et al., 2020. Cortical malformations: lessons in human brain development. Front. Cell. Neurosci. 13. https://doi.org/10.3389/fncel.2019.00576.

Sun, T., et al., 2011. A comparison of proliferative capacity and passaging potential between neural stem and progenitor cells in adherent and Neurosphere cultures. Int. J. Dev. Neurosci. 29 (7) https://doi.org/10.1016/j.ijdevneu.2011.05.012.

Taverna, E., Huttner, W.B., 2010. Neural progenitor nuclei IN motion. Neuron 67, 6. https://doi.org/10.1016/j.neuron.2010.08.027.

Tolić-Nørrelykke, I.M., 2008. Push-me-pull-you: how microtubules organize the cell interior. In. Eur. Biophys. J. 37 https://doi.org/10.1007/s00249-008-0321-0.

Tsai, J.W., et al., 2010. Kinesin 3 and cytoplasmic dynein mediate Interkinetic nuclear migration in neural stem cells. Nat. Neurosci. 13 (12) https://doi.org/10.1038/nn.2665.

Tsai, M.H., et al., 2020. Impairment in dynein-mediated nuclear translocation by BICD2 C-terminal truncation leads to neuronal migration defect and human brain malformation. Acta Neuropathol. Commun. 8 (1) https://doi.org/10.1186/s40478-020-00971-0.

Vallee, R.B., et al., 2009. Emerging roles for myosin II and cytoplasmic dynein in migrating neurons and growth cones. Trends Cell Biol. 19 (7) https://doi.org/10.1016/j.tcb.2009.03.009.

Vives-Bauza, C., et al., 2010. PINK1-dependent recruitment of Parkin to mitochondria in mitophagy. Proc. Natl. Acad. Sci. U. S. A. 107 (1) https://doi.org/10.1073/pnas.0911187107.

Wiggins, L.M., et al., 2012. A novel phenotype for the dynein heavy chain mutation Loa: altered dendritic morphology, organelle density, and reduced numbers of trigeminal motoneurons. J. Comp. Neurol. 520 (12) https://doi.org/10.1002/cne.23085.

Will, L., et al., 2019. Dynein activating adaptor BICD2 controls radial migration of upper-layer cortical neurons in vivo. *Acta Neuropathologica*. Communications 7 (1). https://doi.org/10.1186/s40478-019-0827-y.